Numerical modeling of tsunami waves generated by the flank collapse of the Cumbre Vieja Volcano (La Palma, Canary Islands): Tsunami source and near field effects

S. M. Abadie,[1] J. C. Harris,[2] S. T. Grilli,[2] and R. Fabre[3]

Received 4 October 2011; revised 17 March 2012; accepted 30 March 2012; published 19 May 2012.

[1] In this work, we study waves generated by the potential collapse of the west flank of the Cumbre Vieja Volcano (CVV; La Palma, Canary Island, Spain) through numerical simulations performed in two stages: (i) the initial slide motion and resulting free surface elevation are first calculated using a 3D Navier-Stokes model; (ii) generated waves are then input into a 2D (horizontal) Boussinesq model to further simulate propagation to the nearby islands. Unlike in earlier work on CVV, besides a similar extreme slide volume scenario of 450 km^3, in our simulations: (i) we consider several slide scenarios featuring different volumes (i.e., 20, 40, 80 km^3), which partly result from a geotechnical slope stability analysis; (ii) we use a more accurate bathymetry; and (iii) an incompressible version of a multiple-fluid/material Navier-Stokes model. We find wave trains for each scenario share common features in terms of wave directivity, frequency, and time evolution, but maximum elevations near CVV significantly differ, ranging from 600 to 1200 m (for increasing slide volume). Additionally, our computations show that significant energy transfer from slide to waves only lasts for a short duration (order 200 s), which justifies concentrating our best modeling efforts on the early slide motion phase. The anticipated consequences of such wave trains on La Palma and other Canary Islands are assessed in detail in the paper.

Citation: Abadie, S. M., J. C. Harris, S. T. Grilli, and R. Fabre (2012), Numerical modeling of tsunami waves generated by the flank collapse of the Cumbre Vieja Volcano (La Palma, Canary Islands): Tsunami source and near field effects, *J. Geophys. Res.*, *117*, C05030, doi:10.1029/2011JC007646.

1. Introduction

[2] Large landslides are inherent to the volcanic building process as material continuously accumulates until the point of slope failure [*Holcomb and Searle*, 1991]. Debris avalanche deposits were for instance found in Hawaii [*Moore et al.*, 1989; *Robinson and Eakins*, 2006] or at La Réunion Island [*Cochonat et al.*, 1990; *Oehler et al.*, 2004]. There are also clear geological evidences of past large paleo-submarine landslides of O(100 km^3) volume, around the Canary Islands (Spain). *Masson et al.* [2002] identified at least 14 large landslides, which have occurred on the flanks of the youngest Canary Islands (i.e., El Hierro, La Palma, and Tenerife) in the last one million years, with the youngest one, at El Hierro, being only 15,000 years old. Such potentially catastrophic events may occur in average every 100,000 years in the Canary Archipelago. However, as risk assessment depends upon the product of the probability of occurrence of a given event (e.g., a large landslide and the consequent tsunami) by that of its consequences (e.g., the impact of a large tsunami on the coast), low probability does not necessarily mean low risk. Hence, for proper tsunami impact assessment, the consequences associated with such catastrophic events must be carefully estimated and modeled.

[3] Owing to the large volumes involved, debris avalanches on volcanic islands have the potential for generating very large and energetic waves. For instance, the tsunami triggered during the Shimabara flank collapse in 1792, which caused a debris flow of about 0.5 km^3 [*Inoue*, 1999], killed at least 4,000 peoples. More recently, tsunamis generated by two consecutive small landslides of O(10^6 m^3) (the first being underwater and the second subaerial), during the Stromboli eruption of December 2002 [*Tinti et al.*, 2005], produced local runup values of up to 10 m, without causing any fatalities. Debris avalanches, orders of magnitude larger than these (i.e., up to hundreds of km^3), such as those identified in Hawaii or in the Canary Islands, have the potential for generating vastly more destructive waves (i.e., "mega-tsunami") [e.g., *Ward and Day*, 2001]. While research is still ongoing as of the probability for such large events and associated

[1]SIAME EA 4581, Université de Pau et des Pays de l'Adour, Anglet, France.
[2]Department of Ocean Engineering, University of Rhode Island, Narragansett, Rhode Island, USA.
[3]UMR 5295, CNRS, Pessac, France.

Corresponding author: S. M. Abadie, SIAME EA 4581, Université de Pau et des Pays de l'Adour, Allée du Parc Montaury, F-64600 Anglet, France. (stephane.abadie@univ-pau.fr)

0148-0227/12/2011JC007646

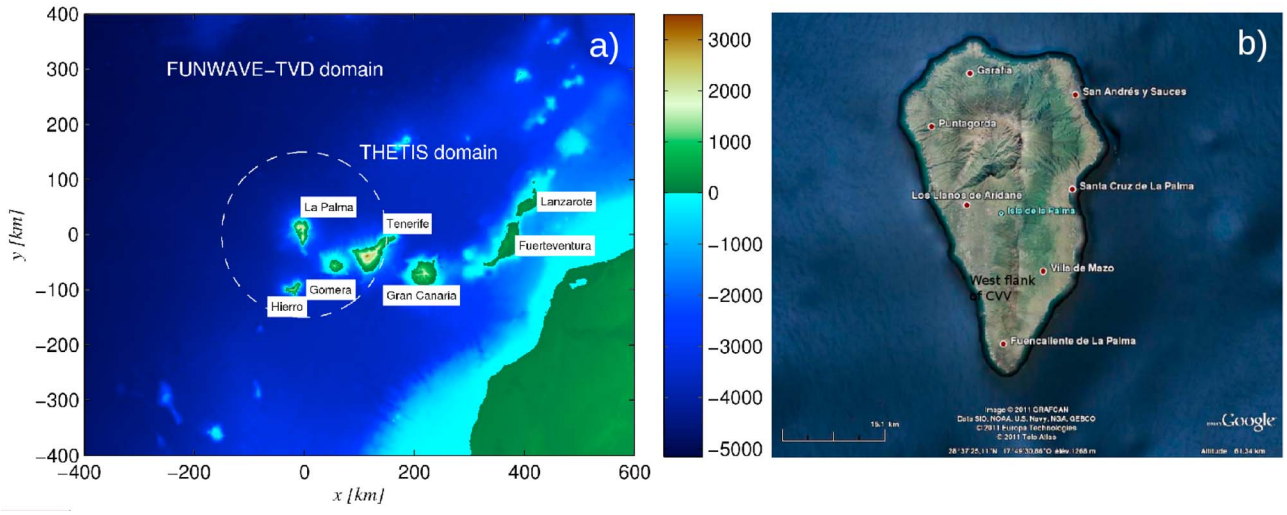

Figure 1. (a) Computational domain covering the Canary Islands, Spain, including the higher resolution THETIS domain surrounding La Palma (28° 37′ 25.11″ N; 17° 49′ 30.86″ W. (b) Details of La Palma Island with most inhabited locations and the study zone.

waves to occur, in the context of comprehensive tsunami impact assessment, one must consider and carefully analyze all large tsunami scenarios that can affect a specific area. The authors are in the process of performing such work along the U.S. east coast, as part of the National Tsunami Hazard Mitigation Program (NTHMP), and results of the present study will be used in the development of tsunami inundation maps. The mechanism by which large volcanic debris avalanches occur (e.g., en masse or in successive stages) plays a key role on wave features and total energy. By analyzing turbidite deposit observations, *Wynn and Masson* [2003] concluded that debris avalanches in the Canary Islands may have occurred in a retrogressive way, which obviously would have reduced their tsunamigenic potential. On the other hand, a few marine deposits found at abnormally high elevations, in Kohala island, Hawaii have been related to debris avalanche and giant waves occurrences [*McMurtry et al.*, 2004]; similar findings were recently reported for the Mauritius Island [*Kelfoun et al.*, 2011]. In the Canary Archipelago, *Pérez-Torrado et al.* [2006] related a marine conglomerate lying between 41 and 188 m on the North-West coast of Gran Canaria, to the nearby Güímar sector collapse (east coast of Tenerife). The latter event was recently modeled by *Giachetti et al.* [2011] and their simulation results corroborated the former assumption. Along the same line, but at a farther location, *McMurtry et al.* [2007] hypothesized that ancient marine sediment deposits found in Bermuda Island were possibly related to a large tsunami caused by a giant Canarian landslide of about the same age.

[4] Among all the volcanoes on the Canary Islands, the Cumbre Vieja Volcano (CVV, see Figure 1b) is the one growing the most rapidly [*Carracedo et al.*, 1999], which hence may pose the largest threat of a flank collapse. The present paper addresses the still remaining question of whether or not a collapse of the CVV West flank sector would generate significant tsunami waves, and to which extent such waves would be destructive in the near-field (i.e., La Palma and other Canary Island shores, see Figure 1a). Far-field propagation and coastal impact of generated tsunami waves (e.g., on the U.S. East Coast) will be detailed in a follow-up paper. This island and more specifically the CVV has been the object of several studies in the past ten years. *Ward and Day* [2001] first brought attention to this potential event and proposed an extreme scenario for the western flank collapse, involving a volume of about 500 km^3. Their simulations resulted in extremely large local waves, which in the far-field still reached up to a 20 m elevation off of the U.S. East coast (particularly in Florida). Both this catastrophic landslide scenario and the wave model used in the work were severely criticized in later work [*Mader*, 2001; *Pararas-Carayannis*, 2002]. Other authors more recently revisited this event, for the same or different slide scenarios, using more accurate models of both landslide and wave generation/propagation [*Pérignon*, 2006; *Grilli et al.*, 2006; *Løvholt et al.*, 2008; *Zhou et al.*, 2011].

[5] Ten years after *Ward and Day*'s [2001] pioneering work, geological scenarios and landslide rupture mechanisms for a CVV flank collapse are still the subject of debate. In the interim, however, significant progress has been made in landslide tsunami simulations, using new advanced computational models. These make it possible to more realistically simulate wave generation by large subaerial (or submarine) mass failures (SMF), once a rupture mechanism has been selected. These SMF models have different levels of complexity and accuracy, depending on which equations are solved. In most models to date, slide motion is prescribed as a moving boundary condition (both shape and kinematics) in a flow solver, which itself may be based on various assumptions, e.g., Shallow Water Wave theory [*Harbitz*, 1992], Fully Non Linear Potential Flow [*Grilli and Watts*, 1999, 2005; *Grilli et al.*, 2002], Boussinesq [*Lynett and Liu*, 2003; *Fuhrman and Madsen*, 2009; *Zhou and Teng*, 2010], or full Navier-Stokes [*Liu et al.*, 2005; *Montagna et al.*, 2011] equations. However, while this methodology is adequate for simple laboratory slide benchmarks that use rigid blocks, it is difficult to apply or at least very inaccurate in natural deforming subaerial slide case studies. In these, indeed, slide motion is impossible to a priori infer, owing to

the complex 3D bathymetry, slide geometry/rheology, and slide/free surface interactions. To this effect, more advanced models must be used, which simulate slide and water flow in a coupled way, and can feature various constitutive laws for the slide phase, allowing to simulate the range of deforming to rigid slides. In such models, again, the accuracy (and related model cost) depends on the set of equations used to describe both water and slide phases. *Jiang and Leblond* [1992, 1993] first proposed such a coupled SMF model, in which (fluid-like) slide and water flows were based on long wave theory, the slide flow being assumed laminar with a parabolic velocity profile a priori imposed. More recently, *Kelfoun and Druitt* [2005] proposed a depth-averaged granular flow model to simulate rock avalanches, for which friction parameters were tuned to reproduce a well-studied historical case study. Later, *Kelfoun et al.* [2010] and *Giachetti et al.* [2011] coupled this model to a shallow water flow model, to simulate tsunamis generated by large debris avalanches. Similarly, *Cecioni and Bellotti* [2010] included a source term in a Mild-Slope Equation model, to simulate landslide tsunami generation, and validated it using experiments for a subaerial slide along the flank of a conical island (modeling the Stromboli volcano).

[6] Strong free surface deformations, with flow separation, large vertical accelerations, and non-hydrostatic pressures, are expected to occur when subaerial or even partially submerged debris avalanches are entering or interacting with water. These phenomena may significantly affect the energy transfer from slide to water flows, and eventually to tsunami waves. Three-dimensional (3D) Navier-Stokes (NS) models, although they are much more computationally intensive than shallow water wave models, can account for multiple fluids (air, water) and materials (rock slide) and, hence, may be the only viable approach to accurately simulate the complex flow processes during initial slide motion, when strong interactions occur with both the water and the free surface flows. Along this line, *Weiss et al.* [2009] modeled the 1958 Lituya Bay slide and tsunami, as a fluid like-granular flow (using experimental information regarding slide processes), in a 2D-NS model. *Gisler et al.* [2006] (see also *Løvholt et al.* [2008]) used a 3D multimaterial compressible NS model, to re-analyze wave generation for *Ward and Day*'s [2001] original idealized CVV slide scenario. This NS solution was then used in *Løvholt et al.* [2008] to initialize a Boussinesq long wave model (BM) and simulate the tsunami transoceanic propagation stages. As expected from other landslide tsunami work [e.g., *Grilli and Watts*, 2005; *Montagna et al.*, 2011], *Løvholt et al.*'s [2008] results confirmed that dispersive effects are important for a realistic description of far field tsunami impact. Landslide tsunamis, indeed, feature relatively shorter wavelengths, as compared to co-seismic tsunamis [e.g., *Watts et al.*, 2003; *Grilli and Watts*, 2005; *Enet and Grilli*, 2007; *Tappin et al.*, 2008], and hence yield more dispersive wave trains, in which wave celerity varies, leading to wave-wave interactions during propagation. This justified using a BM, rather than a more standard non-dispersive long wave model, as was suggested earlier for landslide tsunami modeling [e.g., *Watts et al.*, 2003; *Lynett and Liu*, 2003]. Even though less catastrophic than *Ward and Day*'s [2001], *Løvholt et al.*'s [2008] simulations still predicted very significant wave elevations off of the U.S. East coast.

[7] In this work, we report on the application of an incompressible multifluid 3D Volume Of Fluid (VOF) Navier-Stokes (NS) model (referred to as THETIS) to studying potential tsunamis caused by various scenario of CVV flank collapse. While in this model slides can be deforming with fairly arbitrary rheology, *Abadie et al.* [2010] accurately reproduced the complex coupling between rigid block motion (either subaerial or landslide) and free surface deformation, for a series of laboratory benchmarks, by simulating rigid landslides using a penalty method. In the present paper, the same model is used to study CVV wave generation, but instead of a rigid block motion, a deformable slide is considered. Once waves have propagated away from La Palma, to organize as a radially propagating wave train, with a few leading longer waves, THETIS' ouputs are used to initialize a fully nonlinear and dispersive Boussinesq long wave model (FUNWAVE-TVD) [*Shi et al.*, 2012], which is then used to further propagate the tsunami (Figure 1b). Because SMF tsunamis are made of relatively shorter waves, it is necessary to use a long wave propagation model that simulates dispersive effects and considering the strong nonlinearity of generated waves, one that also includes full nonlinear effects, such as FUNWAVE-TVD [e.g., *Grilli and Watts*, 2005; *Watts et al.*, 2003, 2005; *Enet and Grilli*, 2007]. This work is intended first to revisit and possibly confirm *Gisler et al.*'s [2006] and *Løvholt et al.*'s [2008] simulations of CVV landslide tsunami generation and propagation processes, using different (and perhaps more comprehensive) models of tsunami generation and propagation, and a higher resolution bathymetry and topography. It is also aimed at providing new or more detailed physical insight into slide-wave interaction processes during the wave generation and propagation phases, and to yield a more comprehensive tsunami impact assessment, by simulating several slide scenarios, based on new slope stability analysis of the CVV flank (R. Fabre et al., Potential collapse of the Cumbre Vieja volcanic edifice (La Palma Island, Spain): Numerical investigation of the failure mode and potential volume, submitted to *Engineering Geology*, 2012). The focus of this paper is on wave generation by the CVV collapse, and on near-field tsunami impact on the surrounding Canary Islands. For this reason, owing to the small latitude-longitude extension of the computational grids, the Cartesian implementation of FUNWAVE-TVD is used, with small distance corrections to account for earth sphericity. A follow-up paper will concentrate on far-field propagation and impact of the CVV tsunami, in which the spherical implementation of FUNWAVE-TVD will be used.

2. Slide Scenarios

[8] Slope stability studies along the western flank of the CVV were performed as part of the European research project TRANSFER [*Abadie et al.*, 2008; R. Fabre et al., submitted manuscript, 2012]. The 2D geometrical model (in a vertical plane), for a potential CVV flank collapse and the location of the failure surface were inferred from field data, laboratory tests, and slope stability analyses performed using two different numerical models based on a Mohr-Coulomb failure criterion. By gradually decreasing material property values (thus mimicking hydrothermal alteration), the potential failure surface was identified. A global shear zone, more

or less parallel to the topography and dipping 24° westward, was found based on global plastic indicators and areas of maximum shear strain. Identification of a 2D slide cross-section finally allowed determining slide volume from field data (width and length of semi-elliptical shape). Following this approach, R. Fabre et al. (submitted manuscript, 2012) estimated potential CVV landslide volumes ranging between 38 and 68 km^3, depending on the hypotheses made to assess the lateral extent of any given failure. These values, which are much smaller than that proposed by *Ward and Day* [2001] (i.e., 500 km^3) or used in *Gisler et al.* [2006] and *Løvholt et al.* [2008], appear to be more reasonable, in view of the size of deep water deposits identified at the toe of the volcano, as possibly corresponding to its last massive flank collapse (about 300,000 years ago). These values will be used in the present studies, but the ~500 km^3 extreme scenario will still be simulated to compare with *Løvholt et al.*'s [2008] results. Note, however, that the high safety factors found in Fabre et al.'s (submitted manuscript, 2012) slope stability analyses indicate that the CVV western flank is rather stable under present conditions. Large seismicity and/or a volcanic eruption, however, could nevertheless provide additional destabilizing forces, not included in the latter analyses, that could trigger a slide.

3. Landslide Tsunami Generation

3.1. Landslide Tsunami Generation Model: THETIS

[9] THETIS is a general purpose multifluid NS solver, developed over more than 15 years by the TREFLE CNRS laboratory, at the University of Bordeaux I, France. It is a multipurpose CFD code, freely available to researchers (http://thetis.enscbp.fr). In this section, we give a summary of the application of THETIS to landslide tsunami modeling. More details in this respect, as well as a thorough validation of THETIS for 2D and 3D rigid slide cases, can be found in *Abadie et al.* [2010]. An application of THETIS to wave generation by deformable slides is presented in *Morichon and Abadie* [2010]. Simulations of plunging breaking waves using THETIS were reported in *Abadie et al.* [1998] and *Lubin et al.* [2006].

[10] THETIS solves the incompressible, Large Eddy Simulation (LES), filtered NS equations for water, air, and the slide, considered in this study as a Newtonian fluid, but this is not a limitation as non-Newtonian laws (i.e., Herschel-Bulkley generalized model) can also be used. In the present work, subgrid turbulent dissipation is modeled using a mixed scale subgrid model [*Lubin et al.*, 2006]. THETIS may be referred to as a "one fluid model" since there is no mixing between fluids and only one velocity is defined at every grid cell (by contrast with the two velocities that are for instance defined at the same point for actual two-phase flow models). Thus, at all times, the computational domain is assumed to be filled with one "equivalent" fluid, whose physical properties (namely density and viscosity) vary with space. The governing equations (i.e., conservation of mass and momentum) are discretized using the finite volume method, on a fixed staggered mesh, which may be Cartesian, cylindrical, or curvilinear. These governing equations are exact, except for interfacial grid cells, where momentum fluxes are only approximated, due to the presence of several fluids. All fluid-fluid interfaces are tracked using the VOF method [*Hirt and Nichols*, 1981]. Hence, at every time step the volume fraction of each constituent is known in each grid cell. In locations where interfaces cross grid cells, the fluids' equivalent density and viscosity are simply calculated using a linear interpolation, based on fluid volume fractions. NS equations are solved using a two-step projection method [*Goda*, 1979], in which time step is calculated at each iteration, such that the maximum mesh Courant number is less than 0.5. Once the velocity field is known, fluid volume fractions can be advected using two different methods: (i) the second order Piecewise Linear Interface Construction (PLIC) VOF method [*Youngs*, 1982]; (ii) the explicit Total Variation Decreasing (TVD) Lax-Wendroff scheme of *LeVeque* [1992]. Details of the latter numerical scheme and of its physical validation can be found in *Vincent and Caltagirone* [1999]. The first method keeps interfaces discontinuous, as the advection is based on a geometrical Lagrangian calculation. While accurate, the PLIC algorithm may lead to difficulties or even divergence in the NS solver, when fluid droplets smaller than the grid cell size are generated by the flow. Hence, PLIC was not selected in the present study and advection was based on TVD-VOF. In the latter method, a Lax Wendroff scheme is used to directly solve the purely advective equations governing interface evolutions. In this case, numerical diffusion is expected to occur and slightly smear the interfaces during their propagation. However, *Lubin et al.* [2006] showed that such numerical diffusion is limited to about three grid cells when using a TVD scheme, and that an accuracy comparable to that of the PLIC method may be achieved for the case of solitary wave propagation. Obviously, one may lose some details of the fine interface deformation occurring during violent flows, that cause strong interface deformation, but we consider that such details are of secondary importance, as compared to salient wave generation processes. Finally, note that THETIS has a fully parallelized version based on the Message Passing Interface library. However, in this paper, as some stability problems remained in the cylindrical parallel model, 3D cylindrical computations were still run in sequential mode. For these computations, a BiCGstab iterative solver [*van der Vorst*, 1992], associated to an ILU preconditioner, was used to solve the linear systems.

3.2. Tsunami Generation Model Set-Up

[11] For the tsunami source calculation, bathymetry around La Palma island was obtained by digitizing marine charts, that were created by *Masson et al.* [2002] based on multibeam surveys carried out in 1997. Errors on horizontal distance made during the digitalization process have been estimated to be in the range ±500 m, which would give a global resolution of about 1 km, to be compared to the 2 min resolution (~3,700 m) of ETOPO-2 data previously used in *Løvholt et al.* [2008]. In the model, solid boundaries (bathymetry and topography) are represented as porous media (with zero porosity).

[12] Based on the slope stability analysis results of R. Fabre et al. (submitted manuscript, 2012), four slide scenarios were considered in this study, with initial slide volumes of: 40 km^3 and 80 km^3, consistent with volumes estimated by Fabre et al.; a 20 km^3 lower case scenario; and a 450 km^3 extreme case similar to the scenario studied by *Ward and Day* [2001], *Gisler et al.* [2006], and *Løvholt et al.*

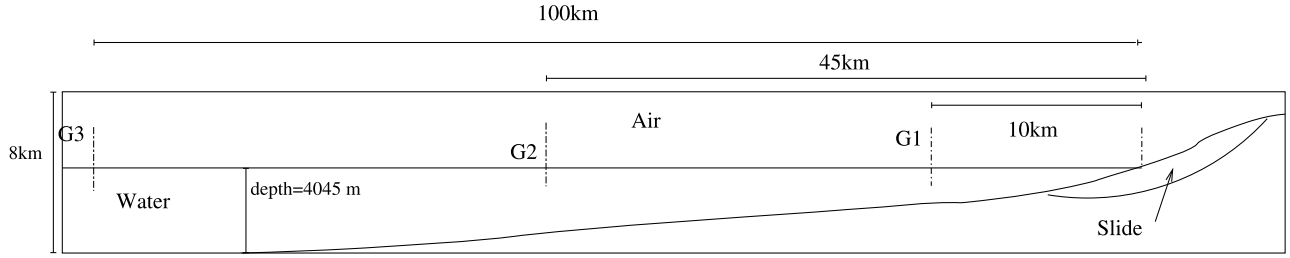

Figure 2. Initial conditions for THETIS 2D simulations with locations of numerical gages G1, G2, and G3.

[2008]. Except for the 450 km^3 case, the slide initial geometry was obtained by taking the intersection between an ellipsoidal rupture surface and the digital terrain model. For the first 3 scenarios, the ellipsoid major semi-axis a is directed North–South, with the two other axes inclined at 17° with respect to the horizontal (minor semi-axis b) and vertical (semi-axis c) directions, respectively, to follow the inclination of the volcano slope. The slide center of mass is located 500 m above sea level, 2.5 km West, and 12 km North of La Palma's southern cape. Specifically, the ellipsoid semi-axis lengths were for the: (i) 80 km^3 case, a = 8 km, b = 4.5 km and c = 900 m; and (ii) 40 km^3 case, a = 7.5 km, b = 4 km and c = 600 m. For the smaller 20 km^3 case, a factor 0.70 (obtained by a trial-error procedure) was applied to each axis length, with regards to the 40 km^3 case. Finally, for the geometry of the 450 km^3 case, the same procedure as detailed in *Løvholt et al.* [2008] was followed. Before performing the more demanding 3D simulations, 2D simulations were first performed in a cross-shore section, that included the 3D ellipsoid center of mass, to more easily study slide processes and select adequate values of numerical parameters (such as grid size) in the model. In this case, the 2D slide rupture surface was defined as the intersection between the 3D slide in the 80 km^3 case and the corresponding 2D cross-shore section, yielding a slide with 8 km length, 900 m thickness, and a 8 km^2 cross section (Figure 2).

[13] Debris avalanches may occur as mixtures of rocks, sediment, water and air; the proportion and distribution of rocks may evolve with time, depending on collision events, local shear, etc. In landslide numerical models, one usually represents these complex processes by an equivalent (heavier) fluid, governed by simple or more complicated constitutive laws [e.g., *Quecedo et al.* 2004]. For practical applications, though, the parameters of the model may be tuned to fit real case observations [e.g., *Hungr*, 1995], usually by taking the run-out distribution as a reference [e.g., *Kelfoun and Druitt*, 2005]. Such an advanced methodology may not be necessary to simulate landslide tsunami generation, for which the majority of wave generation occurs at a fairly early stage of slide motion [e.g., *Grilli and Watts*, 2005], as we shall see later in the CVV study; hence, the subsequent deeper slide dynamics may be less critical to accurately capture in the model. Building a model dedicated to simulating a rock avalanche entering the water would be a challenging task and so far there has not been, to our knowledge, any attempt to do so in the literature. In the present study (following also *Gisler et al.* [2006]), we used the simpler standard approach, in which the CVV slide is considered as an inviscid fluid, with a 2,500 kg/m^3 constant density (i.e., corresponding to basalt). Therefore, in this approach, we do not model basal friction, nor resistance to internal deformation, which should yield more energetic and dynamic slides, likely to generate worst case scenario tsunamis. Results have been reported that support this assumption, indicating that large rock slides have typically large run-out distances, which are incompatible with large friction values (basal or internal) [e.g., *Legros*, 2002]. However, this only applies to the average friction values. Actually, little is known about the basal shear stress behavior and more generally about slide acceleration in the first stage of motion, during which the energy transfer to waves is maximum. Finally, note that internal stresses also control to some extent slide deformability when entering water and later in the sliding process, and hence influence energy transfer rates from slide to free surface waves. There is, however, at this time not enough insight and data in this respect to justify using a more accurate or comprehensive slide constitutive model than the simple proposed inviscid flow model (see for instance the conclusions of *Quecedo et al.* [2004] in this respect). In closing, performing sensitivity analyses of slide kinematics and tsunami generation to slide basal and internal friction will be left out for further investigations.

3.3. CVV Tsunami Generation: 2D Studies

[14] Owing to the typically large size of the tsunami generation area, co-seismic tsunami wave trains generally feature leading long waves (i.e., whose wavelength is on the order of twenty times the local depth or more), with relatively small height (up to one meter in deep water [e.g., *Ioualalen et al.*, 2007]). By contrast, landslide tsunami wave trains such as generated here, generally feature shorter waves, in which frequency dispersion effects may become important [e.g., *Grilli and Watts*, 2005]. This requires using finer resolution grids for their accurate modeling. Accordingly, the objectives of this preliminary 2D study were to: (i) more easily identify an optimal model grid for the more demanding 3D simulations; (ii) investigate wave and slide processes in a relatively simple configuration, yielding less demanding computations. Figure 2 shows a sketch of the computational domain and initial slide used to simulate a 2D CVV flank collapse case in THETIS. The computational domain is 150 km long and 8 km deep. Time series of free surface elevation will be calculated and analyzed at three offshore locations marked on Figure 2.

[15] As NS simulations are computationally demanding, the 3D mesh must be carefully defined to ensure sufficient

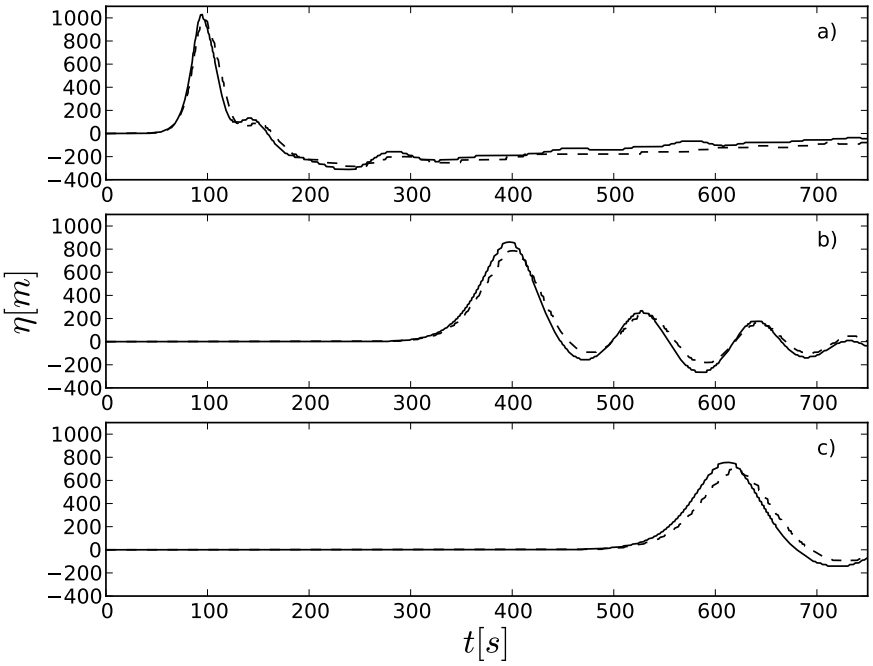

Figure 3. Free surface time history (case of Figure 2) at gage (a) G1 (10 km offshore), (b) G2 (45 km offshore), and (c) G3 (100 km offshore) for two meshes: mesh 1 (solid line) 1500 × 120 (Δx = 100 m, irregular in z), mesh 2 (dashed line) 200 × 80 (irregular in x and z, Δx_{min} = 100 m, Δz_{min} = 10 m).

accuracy and convergence, for the smallest possible grid size. Such grid selection thus requires several trial and error simulations to be run, which are more easily carried out in 2D. The choice of a mesh that is able to correctly reproduce landslide tsunami generation processes is not straightforward. This is mainly due to the fact that, after generation, waves and landslide do not follow the same trajectories and, especially in 3D, the wavefield spatial extent rapidly grows with time. As a first stage (not detailed here), we limited 2D simulations to the immediate generation area, yielding a computational domain that only extended to 30 km offshore [*Abadie et al.*, 2011]. Several meshes were considered (all square, with $\Delta x = \Delta z$), with grid steps ranging from 250 to 40 m. In this first stage, wave elevations in 2D results reached a large maximum of about 1,000 m at gage G1, in part due to the reduced spatial energy spreading in 2D, as compared to 3D. Main tsunami wave features did not show much dependency on grid step, indicating that convergence, in terms of free surface elevation, is quite easily achieved, at least in the generation area [*Abadie et al.*, 2011]. In a second stage, presented here, we simulated wave propagation in the larger domain, extending to 150 km offshore, shown in Figure 2. Our reference solution is calculated using a constant grid step with Δx = 100 m, and an irregular mesh in the vertical z direction (starting with Δz_{min} = 10 m at the free surface; 120 mesh points are used in the vertical z direction and 1,500 in the horizontal x direction. Time series of wave elevation computed at gages G1, G2 and G3 in this finer mesh are plotted as solid lines in Figure 3; the dispersive nature of the generated wave train is apparent on Figure 3. Such a high resolution grid, however, is too fine to be used in full 3D computations. Hence, we will attempt to reproduce the finer grid solution using a coarser irregular 2D grid, defined as an exponentially growing grid, featuring 300 mesh points in the horizontal x direction and starting at the rightward boundary with a minimum step Δx_{min} = 200 m. In the z direction, the grid is reduced to 80 irregular mesh points (to limit computational time in the corresponding 3D simulations), with a minimum step of Δz = 10 m at the free surface. This discretization ensures a minimum resolution of the highest waves (∼1300 m high) of about 100 m at the crest (or trough), while the best resolution of 10 m is specified in the mesh region where waves are propagating the most frequently (i.e., around the seawater level). Figure 3 shows, in dashed lines, the surface elevations computed at the three gages in this reduced mesh. Although differences occur with the finer mesh results, these are quite small (∼1% on propagation time and ∼8% on first wave height at both gages G2 and G3), indicating that this relatively coarser mesh is adequate to achieve sufficient convergence and result accuracy in 3D computations.

[16] Even though, for the considered CVV event, generated waves are very high near the source, the relatively low grid resolution in the z direction will affect model results. For instance, with Δz_{min} = 10 m, one would expect results' accuracy to be at best about 2 or 3 times this value (i.e., 20–30 m) assuming 3 grid cells are required to resolve a wave. To verify this statement, *Abadie et al.* [2011] performed 2D simulations of linear intermediate depth waves, in a periodic domain in the x direction. Free surface elevation and water velocities were specified as initial conditions, based on linear wave theory, and wave amplitudes larger and lower than the vertical grid resolution were simulated over 5 wave periods. Results showed that waves are adequately resolved at least over this time frame even when their amplitude is lower than the model resolution (twice lower was the minimum value tested in this case).

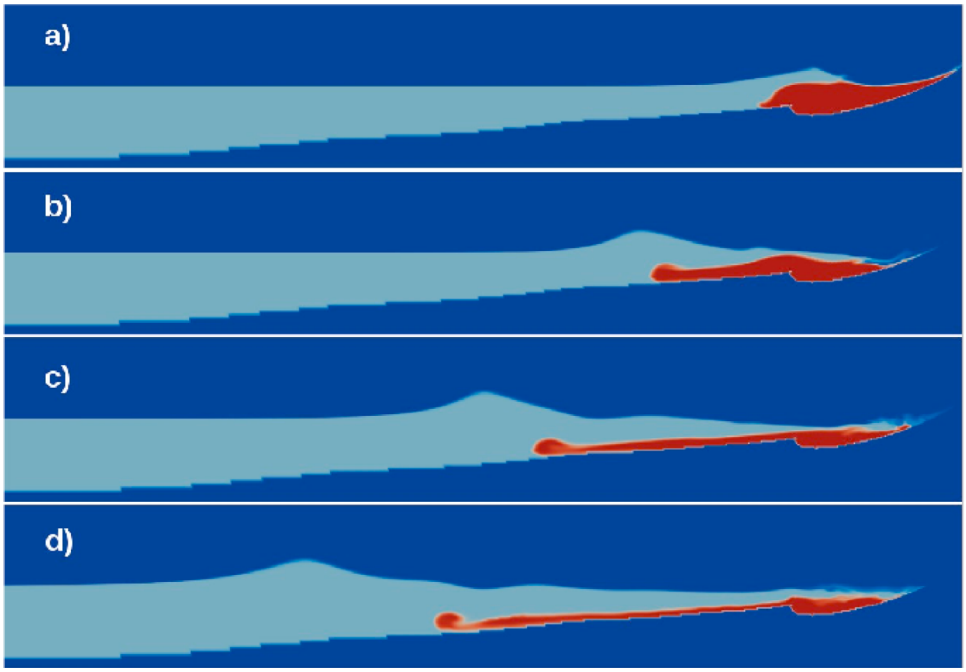

Figure 4. THETIS 2D computations with slide initial surface equal to 8 km^2. Density contours at t = (a) 50 s, (b) 100 s, (c) 150 s, and (d) 200 s.

[17] Figure 4 shows a time sequence of density contours computed at four time steps, using mesh 1 of Figure 3, with a constant Δx = 100 m. Initial conditions correspond to those in Figure 2. We see, the slide flows under the water, as a thin fluid sheet with a bulbous shape front. Several major water waves are generated and propagate (Figures 4b–4d; see also Figure 3b), with the first wave being the highest. Results in Figure 4 also show that a small fraction of the slide material stays trapped at the basis of the elliptical cavity; this will not be the case for 3D simulations. The evolution of the velocity of the slide material (fluid) is plotted in Figure 5a. The maximum mean slide velocity occurs 50 s into the sliding process, at about 80 m/s, while the maximum slide velocity, which occurs within the front half of the slide (leftward in Figure 4), is reached around 100 s after a longer acceleration phase, at about 150 m/s. This value is to be compared to the 190 m/s reported in *Gisler et al.*'s [2006] 2D simulations for a larger slide cross-sectional area of about 12 km^2. Then the slide maximum velocity progressively decreases and levels up at a significant magnitude of 100 m/s. Velocity is significantly non-uniform within the slide fraction, as indicated by the significantly lower value of the mean velocity. The slide local Froude number (i.e., $v_{slide\ front}/\sqrt{gh_{loc}}$) time evolution is plotted in Figure 5b. The Froude number is supercritical (>1) up to about 170 s, which is the time the highest free surface elevation is reached (see Figure 5c), and then becomes subcritical after this time. For such Froude number values, which stay around 1 for a long time, the wave generation process is very efficient and, as a consequence, the maximum free surface elevation can be very large (Figure 5c). Here, this maximum value reaches about 1,300 m, which was also the value found in *Gisler et al.* [2006], but for a larger and faster slide. Finally, we calculated (Figure 5d) the time evolution of kinetic and potential energy for the outward propagating generated waves. We have integrated orbital wave velocities and free surface elevation from the slide tip up to the offshore limit in our computational domain. Results show that the wave mechanical energy quickly increases up to t = 200 s. For later times, the average rate of energy transfer from slide to waves decreases by a factor of 10. Although the slide is still very energetic, the increasing depth drastically diminishes the tsunamigenic potential of the slide. The generation process can be considered to only last for the first 200 s and, therefore, accurate slide modeling may be of importance only for this short time interval. The asymptotic value reached in this calculation represents 30–40% of the slide energy loss at this time. Note that *Gisler* [2008] reported energy transfer values between slide and water of 15–18%, for large shallow submarine slides, and *Fritz et al.* [2004] reported energy conversion rates of 4 to 50% in their subaerial granular slide experiments, taking slide kinetic energy as a reference. In our 2D simulations, from t = 200 s onward, kinetic and potential wave energy appear equally partitioned, as would be expected from standard long wave theory. The 2D wave and slide flows are depicted in greater detail in Figure 6, at t = 396 s (i.e., when the majority of wave generation has occurred). Two clearly distinct water flow patterns appear, on either side of the slide bulb tip. Downstream of the slide tip, long water waves propagate from right to left in quiescent water (see also Figure 4d), while upstream shorter water waves propagate on top of a fairly strong rightward return current (~20 m/s velocity), which affects the whole water column, from the slide tip to the initial slide cavity. Other results would show that the separation streamline between these two flow patterns moves with slide velocity, and these flow patterns persist until the end of the simulation (~1,300 s). The return current is generated as a result of the slide mass input into the

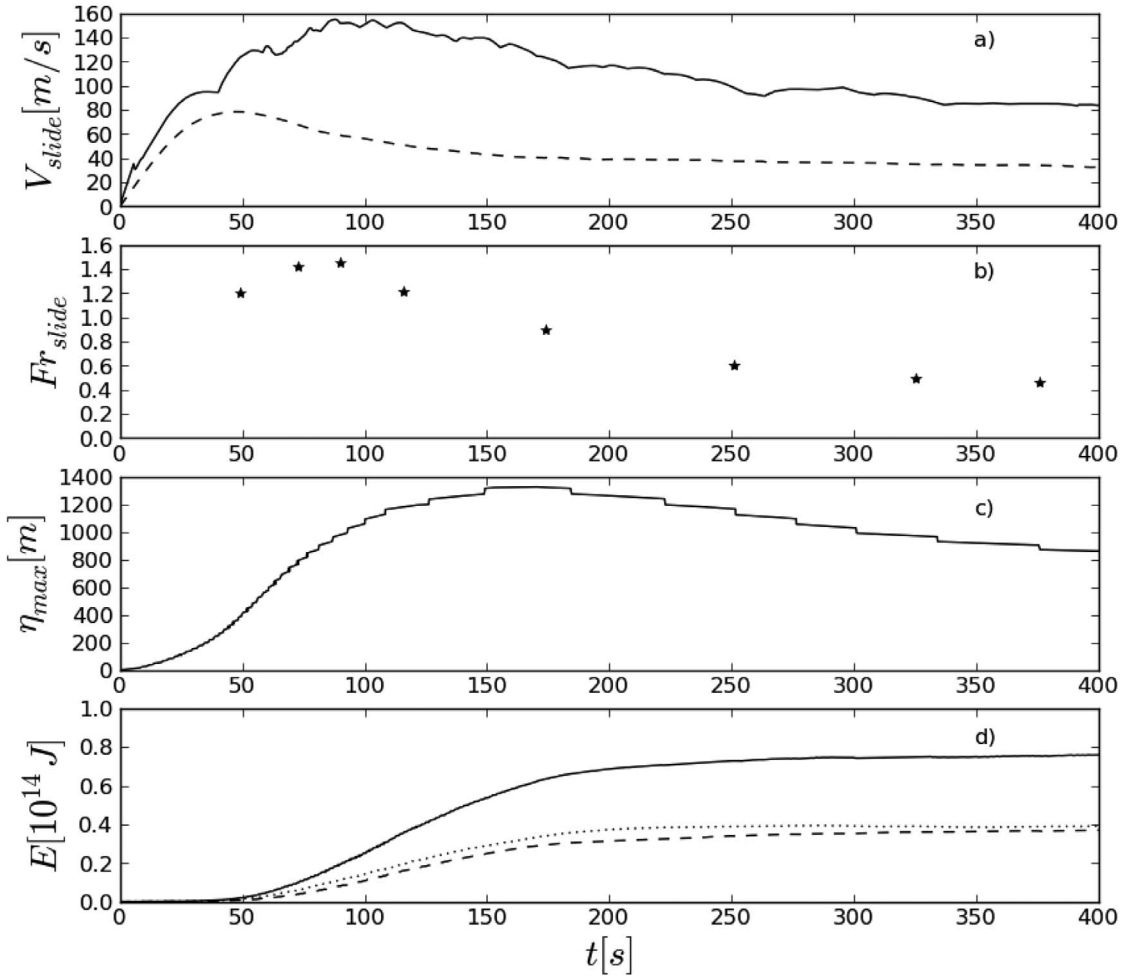

Figure 5. Same case as Figure 4. (a) Slide maximum velocity (solid line), slide mean velocity (dashed line), (b) slide local Froude number, (c) maximum free surface elevation, versus time, and (d) wave energy (solid line), wave potential energy (dashed line), wave kinetic energy (dotted line).

undisturbed water body, which it balances, allowing water to fill the gap left upstream by the slide. As in *Gisler et al.* [2006] and *Løvholt et al.* [2008], we also note in Figure 6 the occurrence of multiple vortices at the interface between slide and water. The largest vortices located at the slide head are related to the slide motion itself, while we attribute the secondary smaller vortices behind the slide tip to Kelvin-Helmholtz (shear) instabilities.

[18] As landslide scenarios have a large intrinsic uncertainty, it is of interest to investigate the sensitivity of wave generation results to a change in slide parameters, given an initial slide shape. Thus, for the same 2D simulation set-up as used so far (shown in Figure 2), we varied slide density, viscosity, and center of mass vertical position, and studied these parameters' influence on: (i) maximum elevation of the first leading wave generated; and (ii) wave energy. Figure 7 (left) shows the maximum computed wave elevation, as a function of slide density; in the range considered in this study, which covers usual rocky slide density values, maximum wave height doesn't show much dependency on slide density. With a density increase of 500 kg/m^3 with respect to the density of basalt (i.e., ~2,500 kg/m^3), maximum wave height only increases by 2.5%, while a decrease by the same amount, causes maximum wave height to decrease by 10%.

[19] By contrast, given a slide density value (i.e., 2,500 kg/m^3), Figure 7 (right) shows that a variation in the slide center of mass vertical position Z_G has a major influence on maximum free surface elevation; this could have been expected since the initial slide potential energy is proportional to Z_G. Results, in Figure 7 (right) were obtained by progressively shifting slide position, following the bathymetric contours, in order to change the slide center of mass altitude, while keeping slide inclination, volume, and thickness constant [note that length was sometimes slightly adjusted in order to meet the preceding constraints]. In the main 2D case considered here (i.e., Figure 4), the slide initial submergence (i.e., vertical distance from free surface to slide center of mass positively counted when directed upwards) is $\delta = 0.05\ h$, where h = 4,045 m is the offshore water depth. With this value, the maximum wave height is about 1,300 m as mentioned previously, and we find that wave height increases at the (high) rate of 1 m per meter of slide submergence. Note that a similar linear dependency was also reported by *Watts* [2000] and *Fine et al.* [2003] in the case of rigid slides. For larger submergence values, the maximum

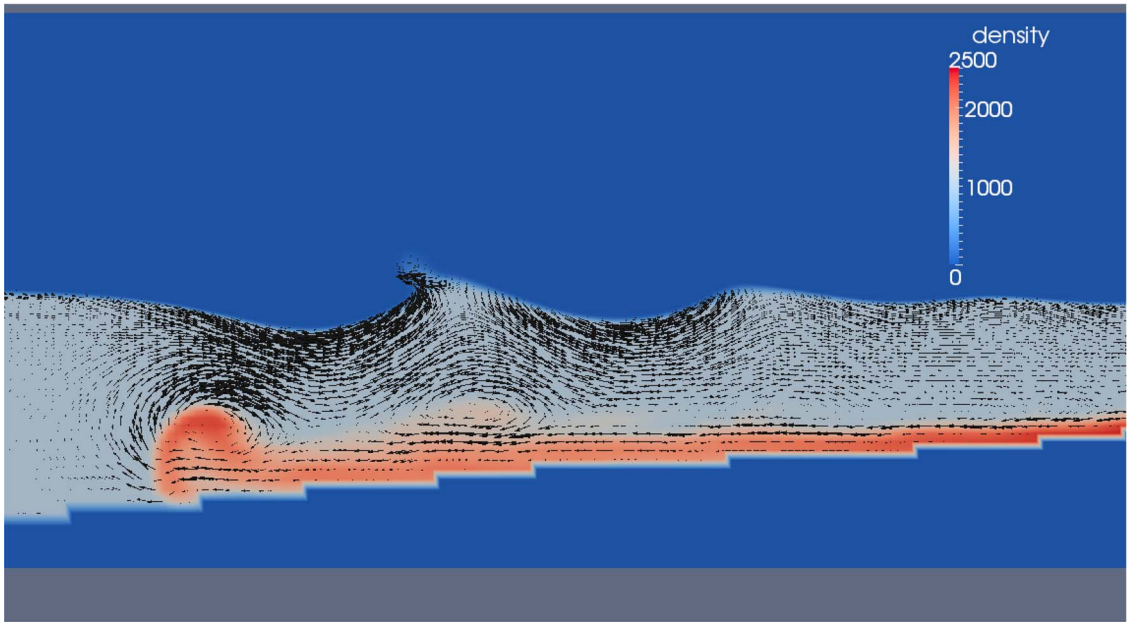

Figure 6. Same case as Figure 4. Detailed velocity field at every other grid around the slide tip at t = 396 s, showing the strong current generated in water by the slide displacement and several vortices at the slide/water interface. Maximum velocities in water are on the order of 100 ms^{-1}.

wave height might reach an asymptotic value, but this conclusion has still to be supported by further work. Thus, in the CVV case, slide initial submergence appears to be a critical parameter for the magnitude of the generated tsunami. We shall see in the next section on 3D simulations, as reported in many earlier studies [e.g., *Fritz et al.*, 2004; *Grilli and Watts*, 2005; *Watts et al.*, 2005], that slide volume is equally important.

[20] Similar to the study of free surface elevation, we investigated next the gradual transfer of slide energy to wave energy (detailed results are not presented here). Asymptotically, wave energy shows a linear dependency to both slide density and center of mass elevation. Finally, the influence of slide viscosity on generated waves was quantified. To do so, we defined the slide Reynolds number, $Re_S = V_S T/\nu$, where V_s is the maximum slide velocity reached over the

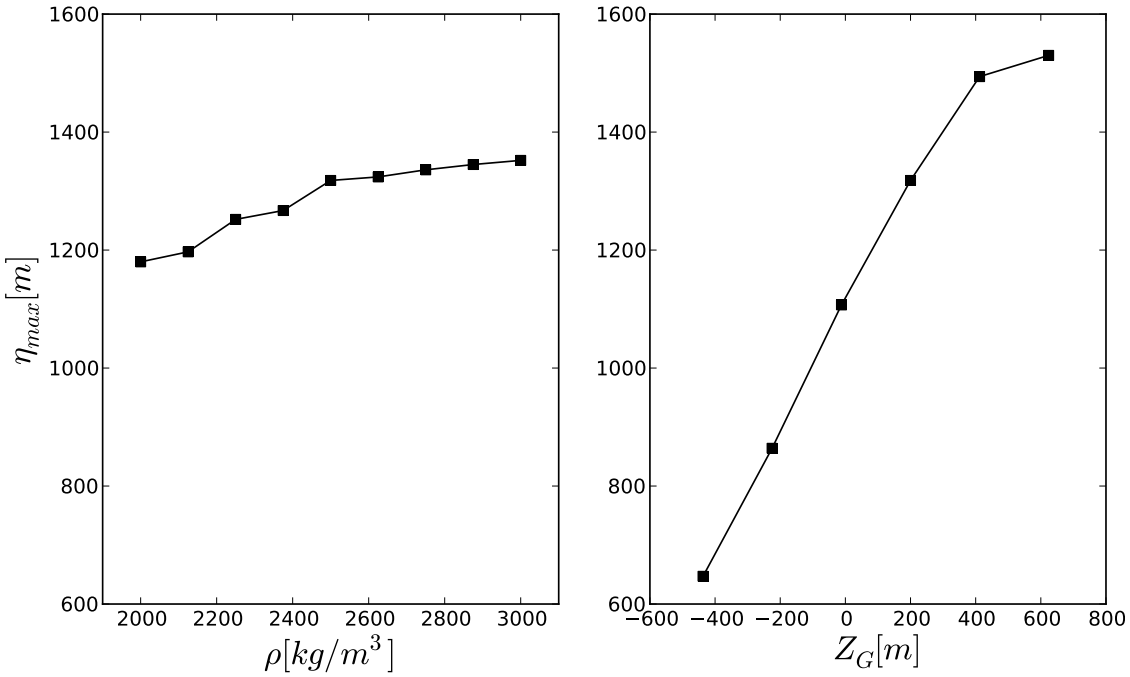

Figure 7. THETIS 2D computations. Variation of maximum free surface elevation with (left) slide density and (right) altitude of slide center of mass with respect to free surface.

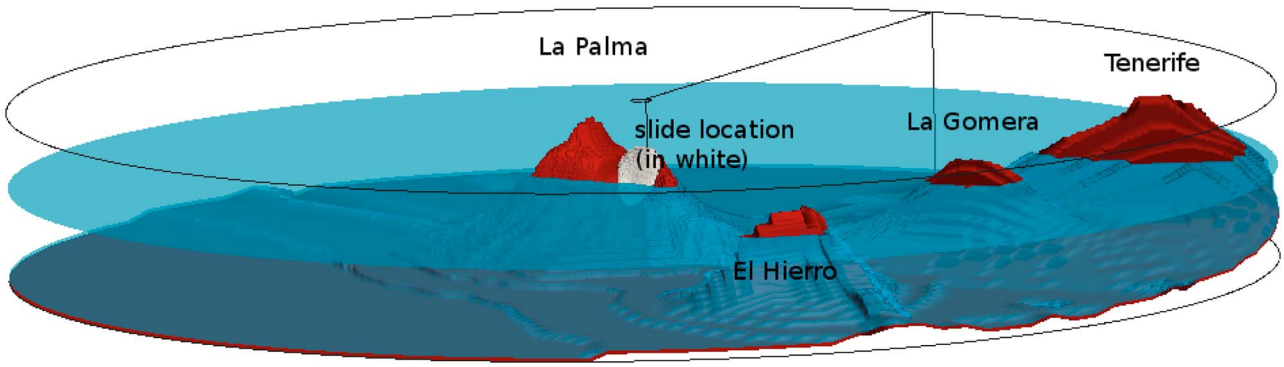

Figure 8. THETIS 3D computations. Snapshot of computational domain with islands and slide location.

simulation, T the slide thickness, and ν the slide kinematic viscosity, representing the ratio of inertia to viscous forces within the slide. Results, not detailed here, show that maximum wave height and asymptotic wave energy both gradually increase with increasing Re_S values, up to $Re_S \sim 10^3$. For larger values, the generated tsunami does no longer show a dependency on slide viscosity, demonstrating (as also stated in *Løvholt et al.* [2008]) that the inviscid slide case (i.e., with a large Re_S value) yields a worst case scenario for Newtonian slide flows, as considered here.

3.4. CVV Tsunami Generation: 3D Studies

[21] Figure 8 shows a sketch of the 3D computational domain for the 80 km^3 slide case, which is discretized with a cylindrical mesh (i.e., whose grid size grows with the distance away from the domain center), to resolve the radial nature of wave propagation with optimal efficiency. The slide area is marked in white on Figure 8. The vertical z coordinate has been exaggerated by a factor of 10, to allow for a better view of the topography and slide position. Besides La Palma island, which appears on the left front part of the picture, three other Canary Islands are included in the computation, which could significantly affect the early stage of wave propagation, and be subjected to high tsunami impact. These islands are from left to right: El Hierro, La Gomera, and Tenerife (the latter being clearly underresolved, as it lays near the outside boundary of the cylindrical mesh). More specifically, the computational domain is a 8 km high cylinder, with a 150 km radius. Based on 2D simulations results, the mesh features 300 grid cells in the radial r direction (with irregular spatial steps, increasing from $\Delta r_{min} = 200$ m in the initial slide area), 80 grid cells in the vertical z direction (with irregular spatial steps, increasing from $\Delta z_{min} = 10$ m at the free surface), and 140 grid cells in the tangential direction θ (with irregular spatial steps, increasing from $\Delta\theta_{min} = 1.2°$ in the approximate direction of the tsunami maximum energy (i.e., 20° anticlockwise with respect to the West direction). With this grid, it takes about one week of computations in scalar mode on a Mac Pro desktop computer (with 64Gb of RAM and two 2.93 GHz 6-core Intel Xeon processors) for 4 min of simulated time.

[22] Figure 9 shows six underwater snapshots for increasing time displaying the simulated air/water and water/slide interfaces for the case with an initial slide volume of 80 km^3, defined by water volume fractions equal to 0.5 and slide volume fractions equal to 0.1. Note the latter value was chosen (rather than 0.5) because, due to the combined effect of mixing and most important shearing (the slide actually gradually transforming into a thin sheet flow), a 50% slide volume rate cannot be found beyond some stage of slide motion. Regarding slide deformation, the bulbous shape taken by the slide front in 2D is similarly observed in this 3D case. The coupling between the slide motion and free surface wave generation is quite clear in Figure 9. In Figure 9c, a very large depression wave, associated with a positive wave (hidden in this view), is generated as a result of the strong initial slide downward motion; this is characteristic of this kind of large subaerial slides. For a long time (Figures 9b–9d), the slide travels nearly at the speed of the leading generated surface waves, allowing for a large transfer of its energy to waves. Figure 10 shows the time evolution of slide characteristics for the same 80 km^3 case. Figure 10a shows slide tip location (i.e., distance to shore) calculated in the vertical plane in the approximate direction of the maximum wave energy. Figure 10b, shows the corresponding slide tip velocity, which reaches a maximum slightly above 100 m/s, which is only two-third of the maximum value found in the corresponding 2D case. This value, reached shortly after slide triggering (i.e., $t = 1$ min), remains at this level until approximately $t = 2$ min. Likely due to 3D bathymetry constraints, slide tip velocity then decreases sharply and reaches about 30 m/s after 3 min of slide motion. From this time to at least $t = 10$ min, slide tip velocity decreases very slowly from 30 m/s to 26 m/s.

[23] The 3D-NS-VOF simulation was not run for a long enough time to allow for an accurate calculation of the slide run-out distance. Based on these results, however, we think that the latter could reach the upper limit of observed run-out values for ancient Canary Island submarine debris avalanches (i.e., 50–130 km after *Paris et al.* [2005]). Indeed, due to the lack of bottom friction (because here the slide is an inviscid fluid), the slide is likely to only stop moving where the bathymetry gradient vanishes. Accordingly, at the end of current simulation, (i.e., at $t = 28$ min; not shown here), the slide tip is 80 km away from shore and still moving with a significant velocity of about 20 m/s. At this time, the slide shape path (not shown here) is very wide, resembling the ancient slide deposit of Playa de la Veta in the same area [*Masson et al.*, 2002].

[24] For wave simulation purposes, there is however no need to accurately simulate the whole slide process. Figure 10c shows the slide Froude number calculated for this

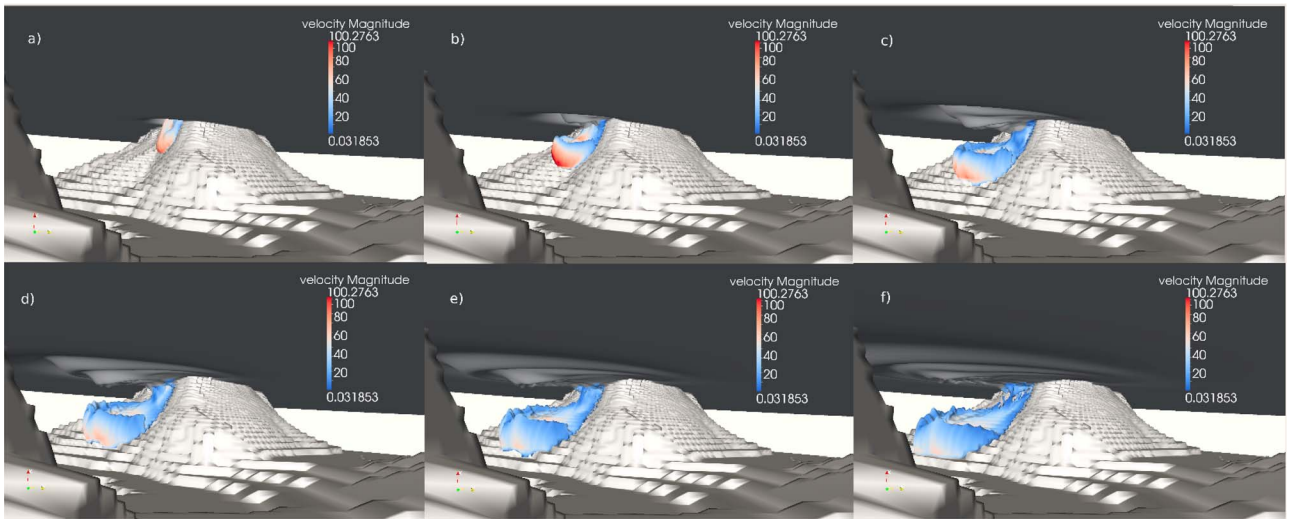

Figure 9. THETIS 3D computations. Underwater view of water and slide interfaces (volume fractions respectively equal to 0.5 and 0.1) at t = (a) 50 s, (b) 100 s, (c) 150 s, (d) 200 s, (e) 250 s, and (f) 300 s for a slide initial volume of 80 km^3. The vertical z coordinates have been exaggerated by a factor of 5, to allow for a better view of the wavefield and slide motion. Slide contour are colored by velocity magnitude.

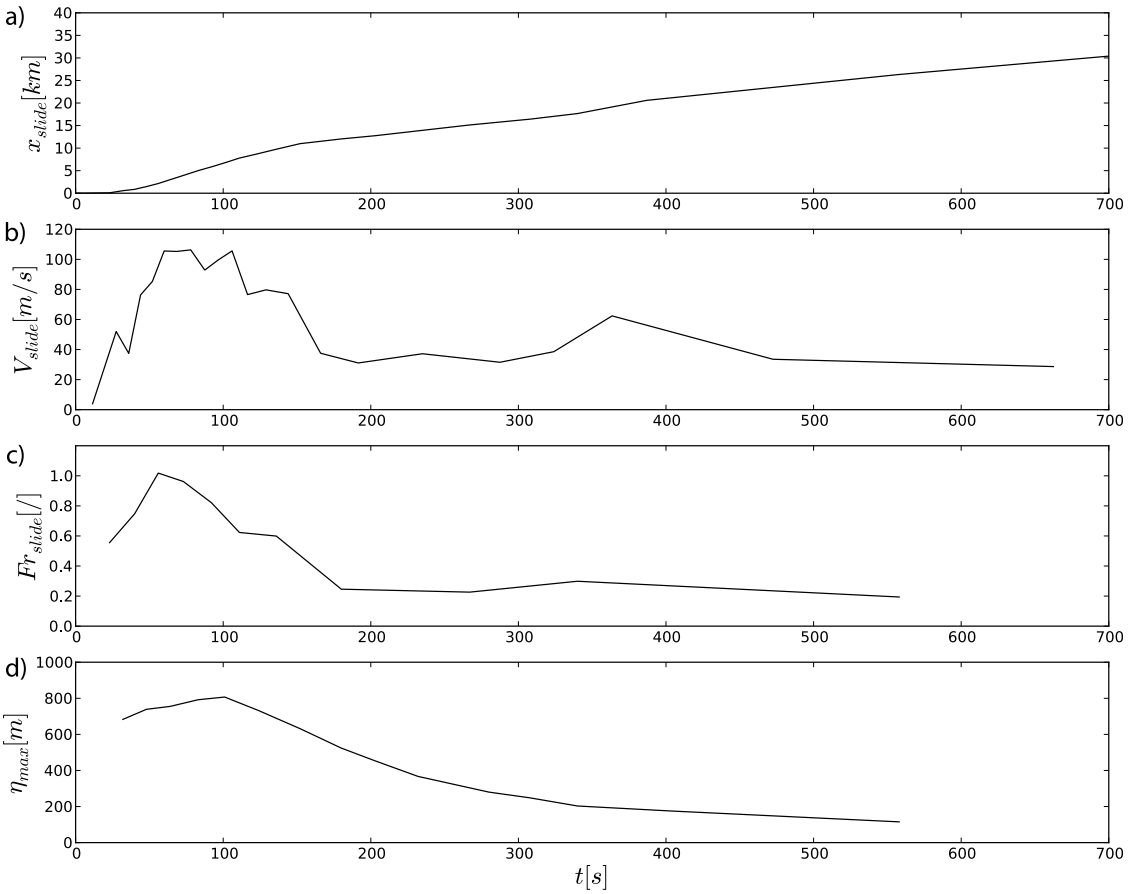

Figure 10. THETIS 3D computations for 80 km^3 slide volume. Evolution of slide characteristics with time in a vertical plane 20° anticlockwise with respect to West: (a) slide tip distance to shore; (b) slide tip velocity; (c) slide local Froude number; and (d) maximum free surface elevation.

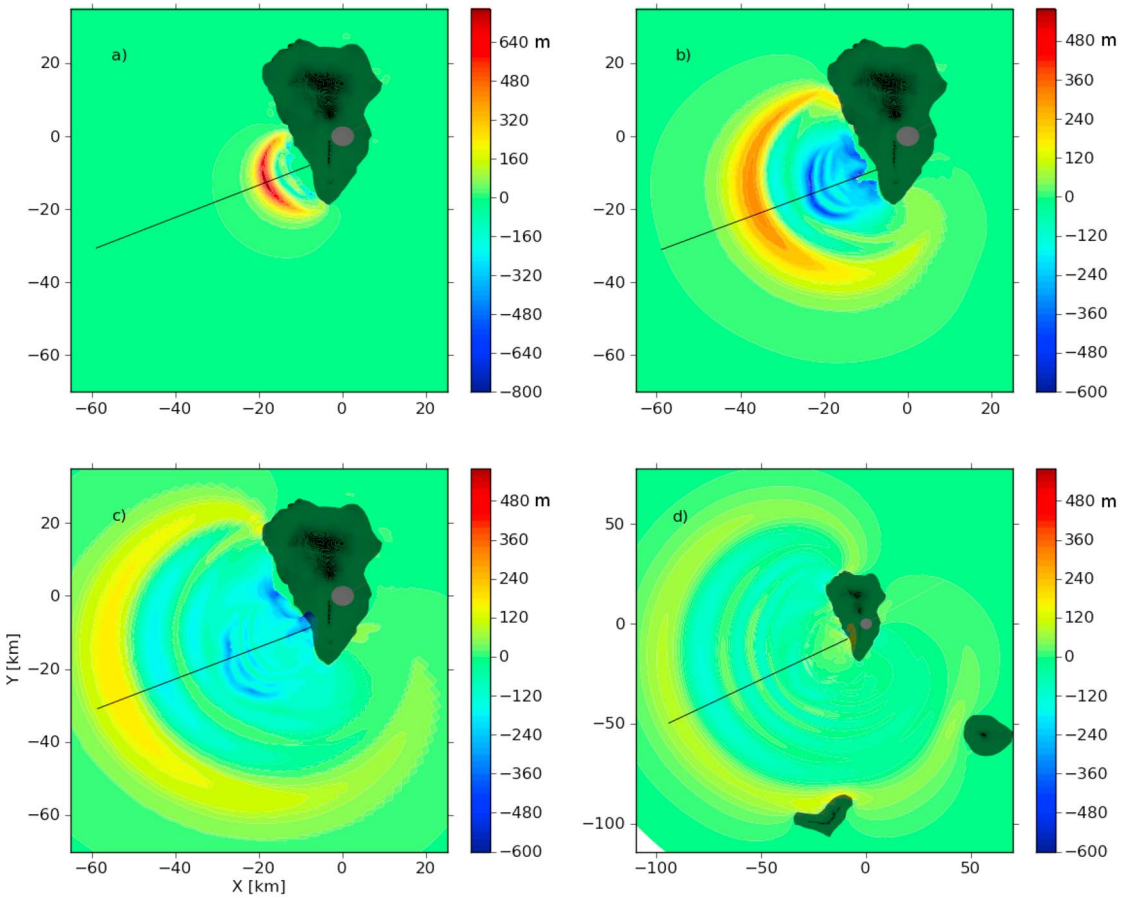

Figure 11. THETIS 3D computations for 80 km^3 slide volume. Contours of wavefield at t = (a) 101 s, (b) 232 s, (c) 340 s, and (d) 558 s. Black lines indicate the main direction of wave generation, 20° south of West.

case, using the local depth. By contrast with 2D simulations, the flow here is only supercritical (synonymous to strong wave energy build-up) for a short time at about t = 1 min., during which most of the wave generation process takes place. Indeed, Figure 10d shows that the associated maximum wave elevation continuously increases until t = 100 s, reaching at this time a maximum value of 800 m (to be compared to 1,300 m in the 2D calculation, where the slide wave generation potential was larger, as demonstrated by the larger Fr values). Slide-to-water energy transfer rates calculated in 2D show that wave energy reaches its asymptotic value as soon as the maximum wave height starts decreasing and Fr $\sim$ 0.7 (only considering waves located beyond the slide tip). In 3D simulations, this would mean that the energy transfer process should be almost over at t = 100 s. Therefore, if tsunami forecast is the goal, modeling efforts should concentrate on simulating wave generation and intense energy transfer during this rather short time interval (t < 100 s in this specific case).

[25] Figure 11 shows free surface elevations computed in the 3D-NS-VOF model at t = 101 s, 232 s, 340 s and 558 s for the same 80 km^3 slide scenario. The color scale is the same in each plot, except in the first plot where it covers a larger range. Additionally, Figure 12 shows vertical cross-sections in the free surface elevations of Figure 11, in the estimated direction of main wave generation (i.e., 20° anticlockwise with respect to the West direction). At t = 101 s, the slide has essentially generated a large leading elevation wave, which reaches about 800 m. In view of 2D simulation results discussed above, energy transfers from slide to waves should be of second order beyond this time, implying that the tsunami generation stage is over. Hence, from this time onward, the initial leading elevation wave propagates freely, radiating away from the island. Due to both 3D (radial) energy spreading and frequency dispersion effects, as time increases, this wave's elevation gradually decreases while an oscillatory tail of gradually shorter and smaller waves develops (Figure 12). While waves propagating faster than the slide are no longer influenced by its motion, the mean water level above and behind the slide is significantly lowered (Figures 11b, 11c, and 12), resulting in a strong run-down at the coast, of more than 300 m at t = 232 s. Because of this phenomenon caused by mass conservation, the free surface elevation behind the leading wave is globally negative and remains so even after a long time of propagation (e.g., t = 558 s; Figure 12). Thus, at t = 558 s, the wave train is composed of an elevation wave, followed by an oscillatory train of lower amplitude waves, whose crests only raise up to near the still water level (z = 0). The direction of propagation of the leading wave evolves with time (Figure 11), starting from about 33° (southwards with respect to the West) at t = 100 s and then shifting to 24°

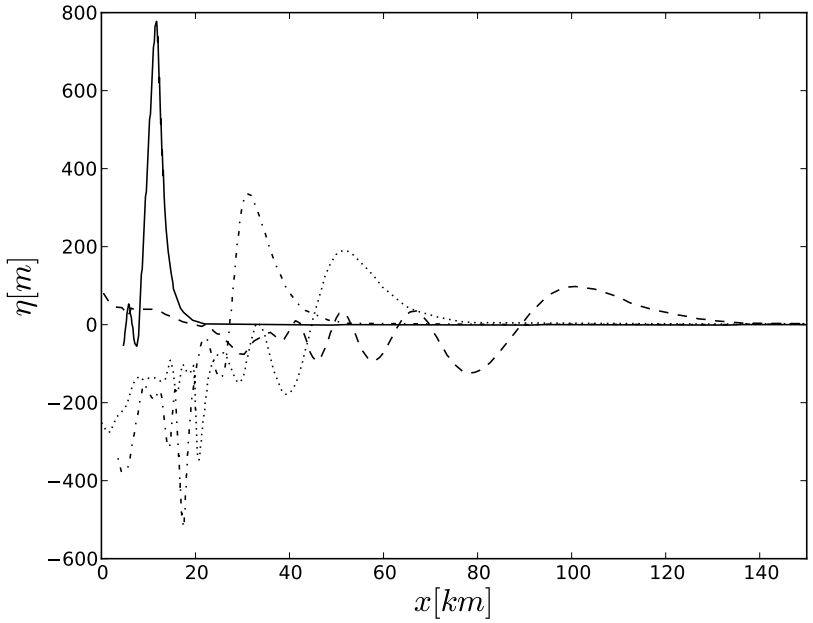

Figure 12. THETIS 3D computations for 80 km^3 slide volume. Free surface elevation in a vertical plane 20° anti-clockwise with respect to West, at t = 101 s (solid line); 232 s (dash-dotted line); 340 s (dotted line); and 558 s (dashed line).

at t = 232 s, and later to 20° at t = 340 s, consistent with previous results [*Løvholt et al.*, 2008]. At later times, neighboring Canary islands (i.e., El Hierro and La Gomera) induce wave diffraction and runup/reflection, which have a significant effect on the angular distribution. Finally, for the 80 km^3 scenario, even though the slide motion is initially westward, significant waves also propagate directly eastward, through diffraction around the southern tip of La Palma, which reach 20–50 m at t = 558 s depending on location (Figure 11).

[26] To better quantify and understand the influence of the source size and geometry on tsunami features, four slide scenarios with different slide volumes of 20, 40, 80 and 450 km^3, were simulated using the 3D-NS-VOF model. Figure 13 shows the wave patterns found for each scenario, just before significant interactions start with the surrounding islands (i.e., at t = 450 s). Overall, the wave pattern is similar in each case, but wave elevations significantly differ: maximum surface elevation at this time reaches 67, 122, 156, and 342 m, in each case respectively. The relatively low difference in maximum elevation (22%), between the 40 and 80 km^3 indicates that initial slide thickness, which is the most significant difference between both of these cases, may only play a secondary role in the wave generation process. All four scenarios also exhibit different behavior in terms of free surface elevation close to La Palma. Obviously, the larger the slide volume, the more pronounced the mean water level depression close to the slide entry location. For the extreme 450 km^3 case, at this time, the water level above the slide, which covers a total area larger than that of the island, is in average about −300 m below still water level.

[27] Despite these differences, the four scenarios share many common features. Figure 13 shows that at t = 450 s, three main leading waves have been generated in all cases. The tsunami directivity is similar (i.e., ∼24° from W at this time), except for the 20 km^3 scenario, for which the highest energy is more westerly directed (i.e., 18°). The average celerity for the first wave tends to slightly increase with initial slide volume. This celerity is 157 m/s for 20 and 40 km^3, 160 m/s for the 80 km^3 case and 173 m/s for the last 450 km^3 case; this could be the effect of amplitude dispersion since the leading wave height grows with slide volume. In contrast, the distance between the first and second wave crests, which is a measure of wavelength, tends to decrease with slide volume: 26.6, 24.4, 23.8 and 21.7 km, in each case respectively. The combination of larger elevation and shorter wavelength yields increasingly steeper, and thus nonlinear leading waves, as slide volume increases. In the latter case, for instance, we get at t = 450 s for the leading wave: H/L = 0.032; kH = 0.20; kh = 0.87 (for depth h = 3000 m) and the limiting steepness is about $(H/L)^{\max}$ = 0.098; hence, the leading wave steepness is about one-third the maximum steepness, and the value of $kh > \pi/10 = 0.314$, the standard limit for long waves, indicating intermediate water waves, for which frequency dispersion effects are important. Other waves in the tsunami train, which are even shorter (Figure 12), have larger kh values and hence feature increasing dispersive effects. Figure 14 shows the build-up and then the decay of the leading wave elevation, with propagation distance, for the four slide scenarios. In this plot, time has been converted to distance using the average wave celerity calculated above and wave elevation transects are computed in the main direction of wave generation, 20 deg. anticlockwise with respect to west. We note again that the 40 and 80 km^3 cases are close to each other in terms of first wave amplitude signal. Maximum wave elevation occurs later and farther away for increasing initial slide volume. The decay rate was quantified by fitting simple power laws based on the least squares method: $\eta = ar^b$, where r is the radial distance traveled by the wave. This

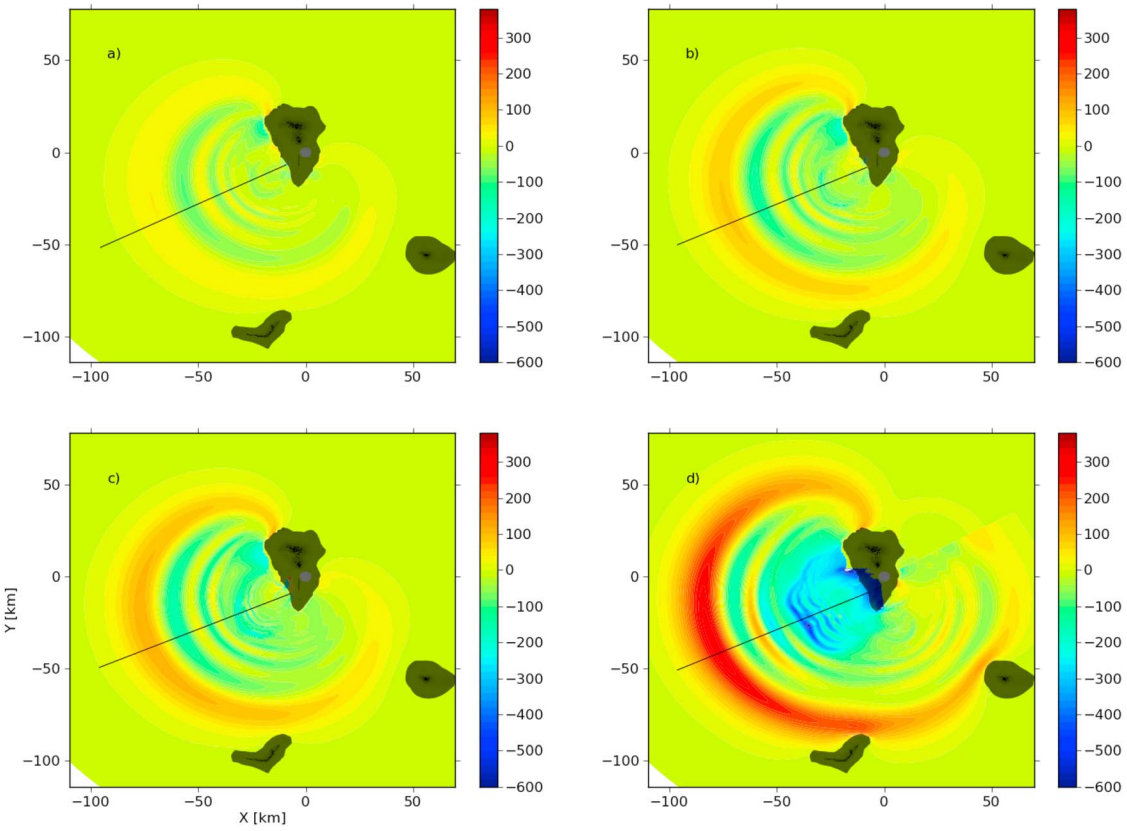

Figure 13. THETIS 3D computations. 2D contours of wavefields at t = 7.5 min, for slide volume of (a) 20 km^3, (b) 40 km^3, (c) 80 km^3, and (d) 450 km^3.

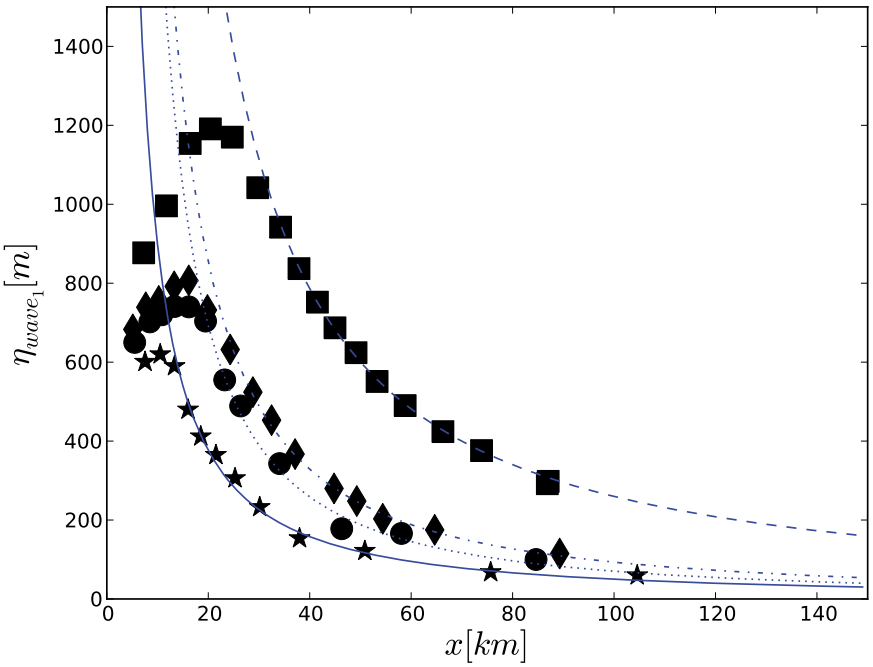

Figure 14. THETIS computations. Maximum wave elevation decay as a function of distance along transects 20° anticlockwise with respect to West, for the four studied slide volume scenarios (symbols). Curve fitted power laws: solid blue line (20 km^3 case), $r^{-1.25}$; dotted blue line (40 km^3), $r^{-1.42}$; dotted-dashed blue line (80 km^3), $r^{-1.38}$; dashed blue line (450 km^3), $r^{-1.21}$.

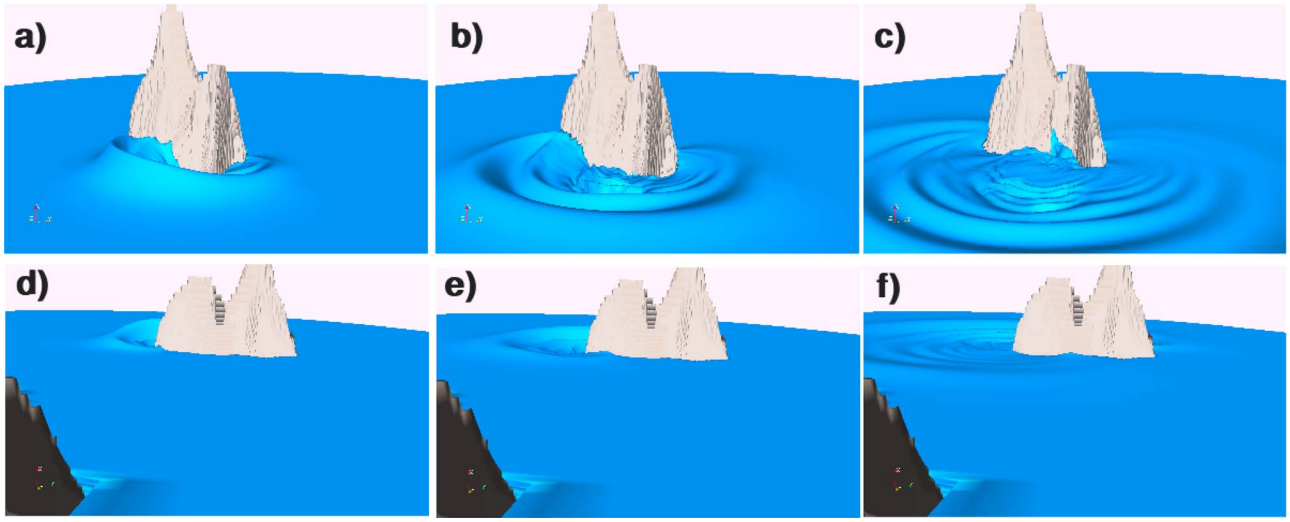

Figure 15. THETIS 3D computations for 80 km^3 slide volume. Wavefield and runup on La Palma. South–West view at t = (a) 192 s, (b) 290 s, and (c) 474 s. East view at t = (d) 192 s, (e) 290 s, and (f) 474 s. Elevation is exaggerated 15 times.

yields the decay rates $b = -1.25$, -1.42, -1.38, and -1.21, for each case, respectively. Such high decay rates, if extrapolated to the far field, would predict a very strong attenuation with distance. Note that even stronger attenuation rates were found in *Gisler et al.* [2006]. The first wave corresponding to the extreme 450 km^3 scenario would for instance only reach 2 m, 5,000 km away from La Palma (roughly the distance from La Palma to North America). But these decay rates should be taken with caution, as near field waves are strongly nonlinear and therefore do not behave as linear waves do in the far field. Moreover, numerical dissipation in the Navier-Stokes model may also contribute to these high initial decay rates. Finally, such near-field power laws do not account for additional wave transformation resulting from far-field wave-wave interactions, and reflections/diffractions occurring during propagation (at islands and various shores), as well as nearshore effects when approaching distant coasts. We shall verify this point in the next section, using the 2D Boussinesq long-wave model to simulate the far-field propagation over larger distances.

[28] Our results can be compared to *Gisler et al.*'s [2006] and *Løvholt et al.*'s [2008], simulations using a multimaterial compressible NS model. As pointed out before, our 2D results are comparable to *Gisler et al.*'s [2006], but in our case they have been obtained with a smaller slide (8 km^2 versus $\sim$12 km^2 cross-section in *Gisler et al.* [2006]), thus involving less initial energy, as evidenced by a slower slide motion. *Gisler et al.* [2006] found a leading wave decay rate $\sim r^{-1.85}$ in their single 3D computation using the SAGE model. Our results yielded a slower decay $\sim r^{-1.21}$, for the corresponding case (our initial slide volume is larger by a factor of 1.2). Note, *Gisler et al.*'s [2006] 3D results were not very detailed in their paper; some information on their maximum wave elevation was found in *Løvholt et al.* [2008]. *Gisler et al.*'s [2006] 2D cylindrical SAGE results showed maximum wave elevations of about 250 m at 60 km offshore, and 160 m, at 80 km offshore *Løvholt et al.* [2008, Figure 3]. Our corresponding values are 470 m and 330 m respectively, hence larger by a factor of 2. Only one result of 3D simulations using SAGE is presented in *Løvholt et al.* [2008, Figure 7]. Maximum wave elevation was about 400 m at t = 5 min, while for this time, we find 560 m with THETIS, which is larger by a factor of 1.4. Finally, *Løvholt et al.* [2008] showed results for wave trains at t = 10 min, using the SAGE solution as initial input into a Boussinesq model (see their Figure 10a). They found a maximum wave elevation for those of about 150 m, while our results again indicate a larger value of 240 m (i.e., by a factor of 1.6).

[29] We studied the runup distribution along La Palma island's coastline, using our 3D-NS-VOF results for the 80 km^3 nominal case. We ensured that, for this case, simulations had been run for a long enough time to capture the maximum runup on the West side of La Palma. On the East side, though, only inundation caused by the leading wave could be computed in the 3D model grid. To study runup on the other Canary islands, which are even more distant from the landslide site and hence are outside the 3D model grid (or have meshes that are too coarse in the cylindrical 3D grid), we will use results of Boussinesq simulations initialized by 3D model results; these will be presented in the next section. Figure 15 shows a time series of snapshots featuring the interaction of the wave train generated by the 80 km^3 slide with La Palma island, seen from a South-Western view (Figures 15a–15c) and from a Eastern view (Figures 15d–15f). The flow interacts with the island in two distinct ways. First, two runups, corresponding to the edges of the radially propagating first wave, propagate alongshore, one around the island by the North and the other by the South. The first runup that starts propagating northward can be seen in Figures 15a–15c; the second one can be seen in Figures 15d–15f. The second phenomenon is a violent backwash generated by the slide motion itself, which can be seen on Figure 15c. At this time (t = 474 s), the (return) fluid flow enters the cavity initially filled by the slide, and generates a large runup. A maximum runup value of 290 m occurs on the northern part of the cavity (Figure 15c). At later times, this backwash also propagates along both sides of the island. Characteristics of both inundation waves are

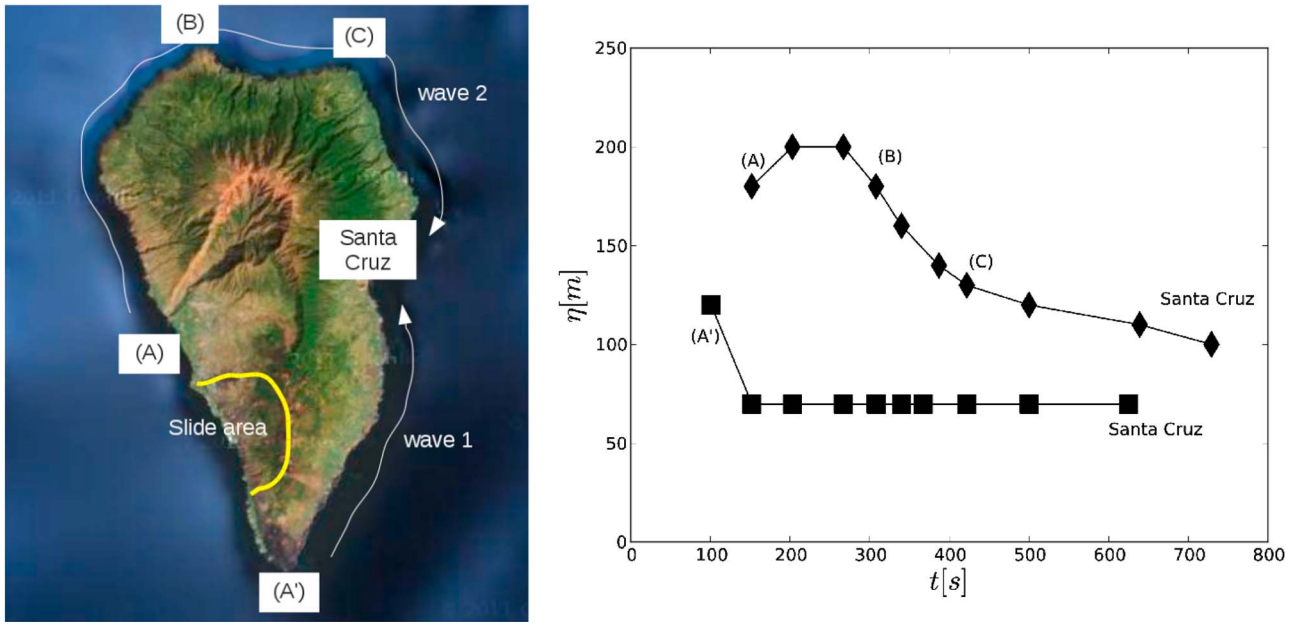

Figure 16. THETIS 3D computations for 80 km^3 slide volume. (left) Sketch of inundation waves paths; (right) time evolution of inundation wave height.

detailed in Figure 16. The path of each wave is sketched on Figure 16 (left) and the maximum amplitudes reached by the leading waves in each train are plotted in Figure 16 (right). The first wave propagating Northward generates a 180–200 m deep inundation on the North–West coast of La Palma. As waves propagate around the island's Northern tip and change direction, after about 12 min. from the start of the event, the largest wave amplitude decreases to about 100 m at the location of the second largest town on La Palma: Santa Cruz (∼18,000 inhabitants), which lies just above sea level. The second wave rapidly decreases in amplitude while changing direction around the Southern tip of the island, and then keeps a constant maximum elevation of about 70 m all the way to Santa Cruz, which it reaches after 10 min. Both inundation waves thus reach Santa Cruz almost simultaneously ($\sim t$ = 10–12 min) strongly interacting afterwards; hence potential damage there would be catastrophic, should this 80 km^3 scenario occur. Note that the town of Los Llanos de Aridane (the largest on the island with ∼20,000 inhabitants), located just right of point (A) in Figure 16 (left) at an altitude of 400 m in average, might be spared the brunt of the tsunami impact in the 80 km^3 scenario, based on our runup calculations.

4. Near Field Effects of CVV Tsunami Waves

4.1. The Boussinesq Model (BM)

[30] As discussed before, it would be too computationally costly to use the 3D model THETIS beyond the region directly surrounding La Palma, for simulating tsunami impact from the CVV flank collapse on neighboring Canary islands and beyond in the far field. Instead, a coupled approach was implemented, in which we use the fully nonlinear (2D-horizontal) Boussinesq Model (BM) FUNWAVE-TVD [*Shi et al.*, 2012], initialized with the THETIS model results. FUNWAVE-TVD is a recent extension of the original FUNWAVE code [*Wei et al.*, 1995; *Kennedy et al.*, 2000; *Chen et al.*, 2000, 2003; *Kirby*, 2003] (see for instance the Appendix in *Ioualalen et al.* [2007] for a summary to date of FUNWAVE's equations and numerical methods). Originally, FUNWAVE was designed and used for modeling coastal and nearshore waves, but it was later successfully applied to a variety of tsunami case studies, both landslide and co-seismic [e.g., *Watts et al.*, 2003; *Day et al.*, 2005; *Grilli et al.*, 2007; *Ioualalen et al.*, 2007; *Tappin et al.*, 2008; *Mård Karlsson et al.*, 2009; *Grilli et al.*, 2010, 2012] A fully nonlinear BM can simulate more complete physical phenomena, especially dispersion, than models based on Nonlinear Shallow Water Equations (NSWE), which are traditionally used for modeling co-seismic tsunamis. This is particularly important for simulating landslide tsunami propagation, for which waves, as indicated above in the CVV case, are in the intermediate-depth dispersive regime ($\pi/10 < kh < \pi$). Improved runup and inundation predictions can also be achieved in a BM, because of the better representation of wave-wave interactions in tsunami wave trains.

[31] In the present work, the latest version of FUNWAVE is used, which is referred to as FUNWAVE-TVD, as it uses a combined finite-volume and finite difference MUSCL-TVD scheme. It is based on the equations of *Chen* [2006] and *Shi et al.* [2012]. As in FUNWAVE, in order to approximate linear dispersive properties up to the deep water limit [*Wei et al.*, 1995], the Boussinesq equations are expressed in terms of the horizontal velocity components at 0.531 times the local depth. In FUNWAVE-TVD, wave breaking is more accurately modeled by switching from the Boussinesq equations to the NSWE, when the local Froude number exceeds 2.0 and/or the height to depth ratio exceeds 0.65. FUNWAVE-TVD's latest implementation was fully parallelized using MPI, for use on distributed memory clusters, by using domain decomposition. (Note, the model

used here did not perform any type of mesh refinement, although one-way nesting has now been implemented in the latest FUNWAVE-TVD version and will be used in a follow-up paper to simulate transoceanic tsunami propagation from CVV scenarios.) The model was fully validated using all of NOAA's National Tsunami Mitigation Program (NTHMP) mandatory benchmarks as part of a model benchmarking workshop organized by NTHMP in March 2011. In the CVV case study, in order to capture inundation and runup on La Palma, a high resolution grid is required in the near-field, but as depth rapidly drops off to around 4.5 km offshore of the island, the intermediate-depth and even shorter trailing waves (with $kh > \pi$) in the radiating tsunami train must be accurately resolved. This justifies using an extended Boussinesq model, such as FUNWAVE-TVD (4th-order in kh), which can closely approximate (linear) frequency dispersion effects at least up to $kh = \pi$. When restarting FUNWAVE simulations using THETIS results, however, it was found that the standard 4th-order MUSCL scheme eventually became unstable, but that a 3rd-order scheme (which still generates 4th-order accurate results) worked well for all model setups presented below; hence, this 3rd-order scheme was used in the present simulations. In the latter, for the wetting and drying scheme along shoreline boundaries, we used a minimum depth of 0.01 m and, to simulate bottom drag, a 0.01 friction coefficient was used up to a minimum depth of 0.10 m, to prevent extremely high bottom friction values from occurring. Finally, at the time this work was performed, a fully nonlinear version of FUNWAVE-TVD was only available for Cartesian grids, while the spherical implementation was only weakly nonlinear. Considering the fairly small latitudinal and longitudinal extent of FUNWAVE's near-field simulation domain (Figure 1a), the former grid was used, with distance corrections to account for spherical effects (see below).

[32] Ocean bathymetry from the Global Multi Resolution Topography (GMRT) database [*Ryan et al.*, 2009] (Figure 1a) was used in FUNWAVE's simulations, which is a gridded digital elevation model with variable resolution depending on available data. This yields an improvement over *Løvholt et al.'s* ETOPO2 bathymetric data (which only has a $2' \times 2'$ resolution), since the GMRT data around La Palma includes the actual bathymetry from *Watts and Masson* [1995], which is of much higher resolution, while ETOPO2 is only based on gravitational anomalies (both too coarse and known to be in error near landmasses). While THETIS used the same high-resolution bathymetry near La Palma as FUNWAVE, because of the different grid interpolation schemes there were slight differences in the bathymetry used by the two models. This was shown to have negligible effects on results, as will be detailed below in the validation of the initialization process. As indicated, in order to take advantage of the fully nonlinear version of FUNWAVE-TVD that is required to accurately compute coastal effects, a Cartesian coordinate grid system is used. To correct for earth's sphericity, a transverse secant Mercator projection is used (similar to the UTM system), with its origin at 28.5 N and 18.5 W (corresponding to −69 km, −14 km). This transformation leads to some small grid distortion, which are however deemed negligible. (The finest resolution grid used here has a 500 m undistorted mesh size; after the coordinate transformation we find that the largest distance between adjacent cells is 502.1 m, and the smallest distance is 496.4 m, giving a distortion of less than one percent, which we consider to be acceptable.)

[33] Figure 1a shows the full extent of the FUNWAVE grid used in the near-field simulations. A 100 km thick sponge layer is applied to the outside boundaries to prevent reflection from corrupting model results. In order to allow for sufficient time for waves to reach the eastern side of the farthest Canary Islands (i.e., Arrecife on Lanzarote), in all slide cases, FUNWAVE simulations were run for 2 h, with a time step that is adaptively set to force the CFL number to be near 0.5.

4.2. Validation of THETIS' Initialization of FUNWAVE

[34] The coupling of THETIS with FUNWAVE is performed by using the 3D-VOF-NS solution at $t = 300$ s as an initial condition for FUNWAVE; i.e., this is a one-way coupling. Although at $t = 300$ s the slide has not yet come to a stop and there is still turbulent flow in the domain, this time is after nearly all of the energy transfer from slide to waves has occurred (Figure 5) and before the leading edge of the tsunami has reached the edge of the THETIS domain. To satisfy mass conservation in the BM, the NS velocity field is first depth-averaged, and its horizontal components, together with the free surface elevation, are interpolated onto the FUNWAVE mesh (Figure 17a). This results in a slight error (2nd-order in kh), as the BM equations are framed in terms of a single horizontal velocity at a reference depth, but this has little effect on the results and has the advantage of averaging out the turbulent flow in the vertical direction. As seen in THETIS's 3D results (e.g., Figures 9f, 15c, 11d, 12, 13d), the tsunami wave train generated by the CVV slide, after a series of 3–4 larger and longer, long-crested, leading waves, features very short and irregular trailing waves, which result from the 3D highly turbulent residual flow induced by the slide near its initial location in La Palma. This turbulent flow (see e.g., Figure 6) is initially associated with short waves, but vertical mixing, which is most active around the slide tip, dissipates this flow without transferring energy to the wavefield. As this flow is not responsible for any significant tsunami coastal impact on either La Palma or more distant islands, and cannot be accurately represented in the BM, it seems reasonable to filter the NS solution prior to using it for initializing FUNWAVE. An ad hoc filtering method (Figure 17b) was determined through numerical experimentation, which consisted in multiplying the output of THETIS (i.e., free-surface elevation and each velocity component) by a spatially varying function (Figure 18), removing the interior flow while keeping a smooth initial condition for FUNWAVE. This function is Gaussian, with a standard deviation of 15 km and the center is located at coordinates (−10 km, −10 km).

[35] Prior to performing longer-term propagation simulations in FUNWAVE, we verified that this coupling approach provided reasonable initial results, for at least the first few leading waves, since most of the runup and inundation will be caused by these waves. This was done by initializing FUNWAVE using THETIS' results at $t = 300$ s and performing simulations with both models for an additional 250 s. Free surface elevations computed in both models are then compared at $t = 550$ s in Figures 19 and 20. To assess the effect of the filtering method of THETIS results,

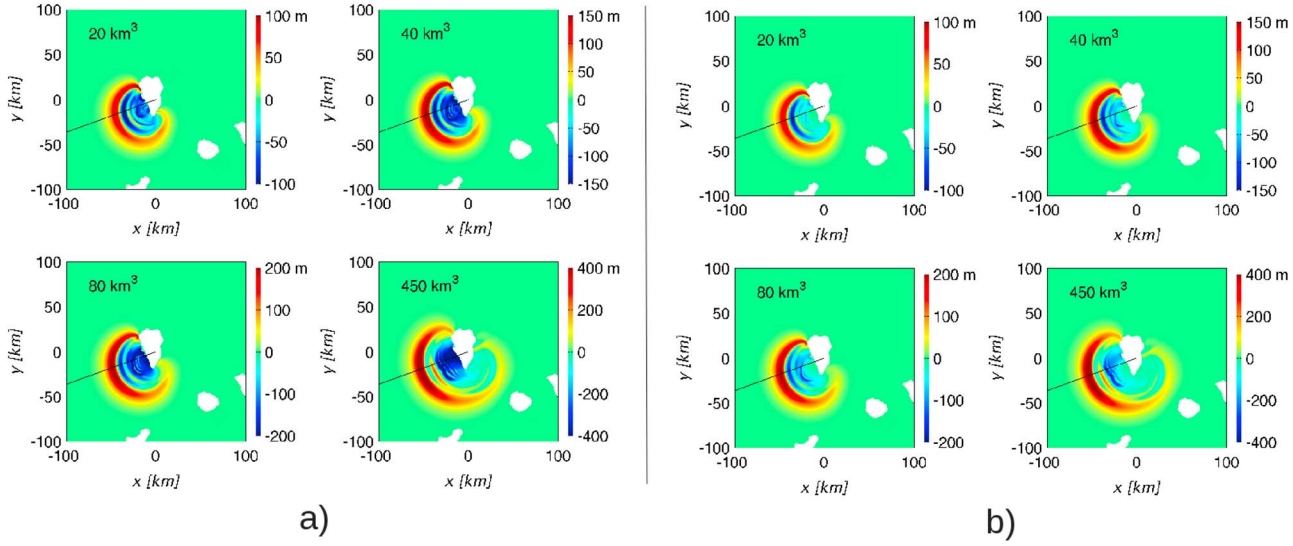

Figure 17. Initial conditions used in FUNWAVE computations (a) before filtering; (b) after filtering.

FUNWAVE computations were performed using both unfiltered and filtered THETIS results. The main direction of wave propagation, 20° anticlockwise with respect to west, along which transects in Figure 20 are made, is marked by thin black lines in Figure 19. Note that, in Figure 19, there is a slight difference in the water level in the far-field between the THETIS and FUNWAVE-TVD results, which is an artifact of processing the THETIS results. Considering the depth and resolution of the models, this has a negligible effect on the results.

[36] Although, FUNWAVE's unfiltered results (Figure 19, left) appear reasonable as compared to THETIS' results, as expected, there is not enough nearshore dissipation of shorter waves; besides causing unrealistically large short waves to appear near La Palma, this also affects at least the 3rd leading wave in the tsunami train. This is greatly improved in FUNWAVE's filtered results (Figure 19, right), which compare well to THETIS' results; we see that both the large short waves near La Palma dissipate and the 3rd leading wave now agrees well with THETIS results. This is even more apparent along transects of the same results at t = 550 s, shown in Figure 20. While the 1st leading wave is essentially identical in all three cases, the second and part of the third wave are also well matched, between FUNWAVE's (filtered or unfiltered) and THETIS's results; the large shorter trailing waves that are near La Palma in FUNWAVE's unfiltered results have clearly disappeared in the filtered results. It should be noted that the filtering has the incidental effect of removing a large surface depression wave near the slide tip (see Figures 11b and 11c), but this depression mostly dissipates by t = 550 s in THETIS's results, and any disturbance caused by this removal will propagate at speeds no faster than the leading waves; hence it is unlikely to affect the propagation of the tsunami significantly. While results are only shown for the 80 km^3 slide, it was verified that the overall quality of

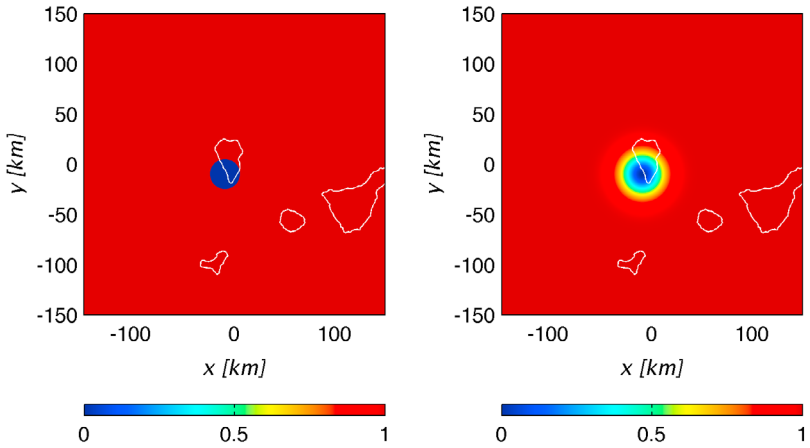

Figure 18. Filtering function (Gaussian hump with a standard deviation of 15 km, and a center located at (−10 km, −10 km) in the local coordinate system), multiplying wave elevation and horizontal velocity prior to applying the initial conditions of (right) FUNWAVE compared to (left) simple distance criterion. Note that if a function like that on the left was used, very sharp edges would exist in the initial condition.

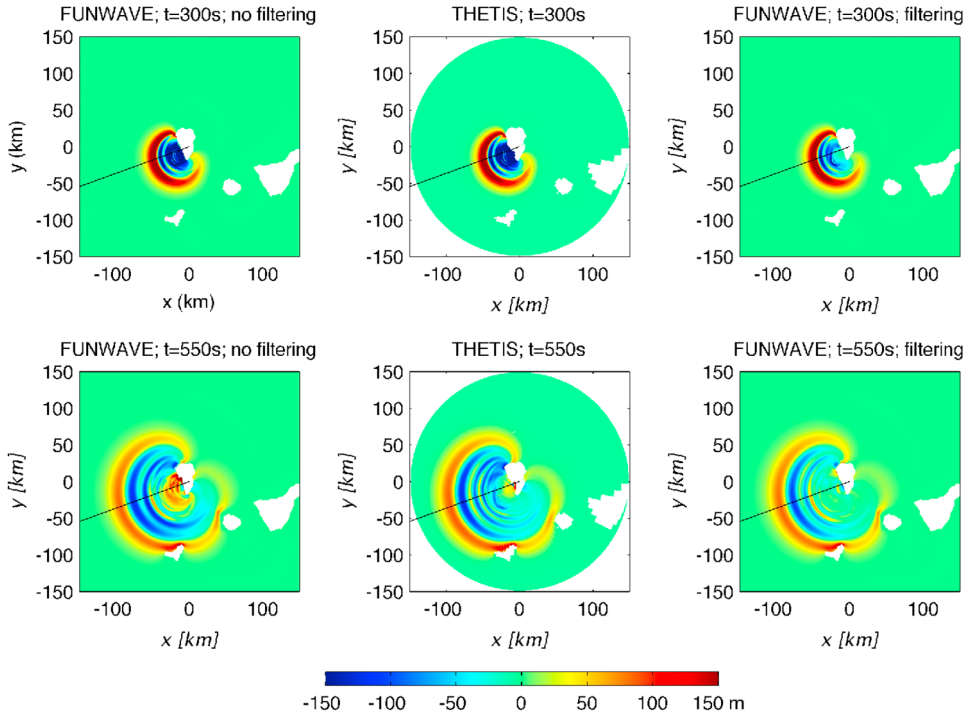

Figure 19. Test of model coupling for the 80 km^3 case, when modeling wave propagation from $t = 300$ to 550 s using (left) FUNWAVE without filtering the initial conditions; (middle) THETIS; and (right) FUNWAVE with filtering the initial conditions. The main direction of wave propagation, 20° anticlockwise with respect to west, along which transects in Figures 20, 21, 25, 26 are made, is marked by thin black lines.

the comparison is similar for all four scenarios. Using the THETIS filtered results to initialize FUNWAVE, we then assessed in Figure 21 the effect of FUNWAVE grid resolution on result accuracy, by analyzing similar transects at $t = 25$ min. (i.e., after 20 min. of propagation in FUNWAVE). We see that, with a decreasing resolution in the BM from 500 m to 2000 m, one still simulates quite well the amplitude and shape of the 1st and part of the 2nd leading waves, but the trailing dispersive wave train is gradually damped. In the following FUNWAVE simulations, although even the

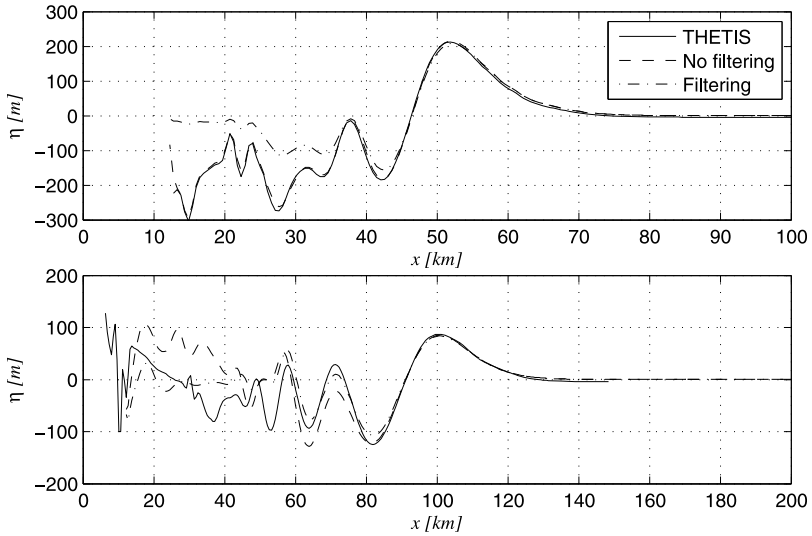

Figure 20. Transects (see Figure 19) of surface elevation at (top) $t = 300$ s and (bottom) $t = 550$ s, as a function of the westward propagation distance. Results show the effects of filtering in FUNWAVE. Note the slight difference in the surface elevation far from La Palma – this is due to a slight artifact of the post-processing of the THETIS results, which is removed before initializing the FUNWAVE model.

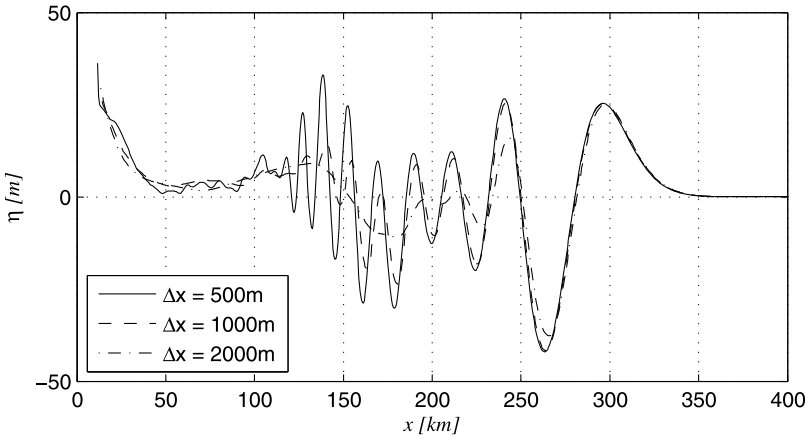

Figure 21. Transects (see Figure 19) of surface elevation at t = 25 min., as a function of the westward propagation distance. Results show the effects of different grid resolution, from 500 to 2000 m.

1000 m resolution grid predicts very similar results for the first four waves of the tsunami, we use the more accurate 500 × 500 m grid. Note that more important than controlling the exact form of the tail, dispersion has a significant effect on the leading waves. The results from *Løvholt et al.* [2008] with a qualitatively similar wave showed that a non-dispersive model would overpredict the tsunami amplitude in comparison with a BM, and produce steeper waves that would break earlier.

4.3. Near Field Impact of CVV Tsunami

[37] Coupled THETIS-FUNWAVE-TVD results, such as shown in Figure 22a, are used to compute near-field tsunami impact on the neighboring Canary islands, due to the various CVV flank collapse scenarios. While Figure 22a shows that the majority of wave generation and propagation occurs in a general westward direction, there is also a significant eastward propagation of sizable waves, which can severely impact neighboring islands, owing to their proximity, as well as the west coast of Africa (not detailed here). To estimate this impact, we computed the tsunami propagation times and maximum wave heights at various major cities on neighboring Canary Islands. Although FUNWAVE-TVD can predict wetting and drying at the coastline, the 500 m resolution is insufficient to accurately map inundation of specific cities. Hence, we present instead the maximum water elevation computed offshore of seven major cities (Figure 22b). Figure 23 shows the waves as they impact the islands of Gomera and Tenerife. Wave run-down around Gomera (Figure 23, left), among other islands, may be poorly resolved, but this is unlikely to significantly affect the maximum wave height. Time series of the 500, 1000, and

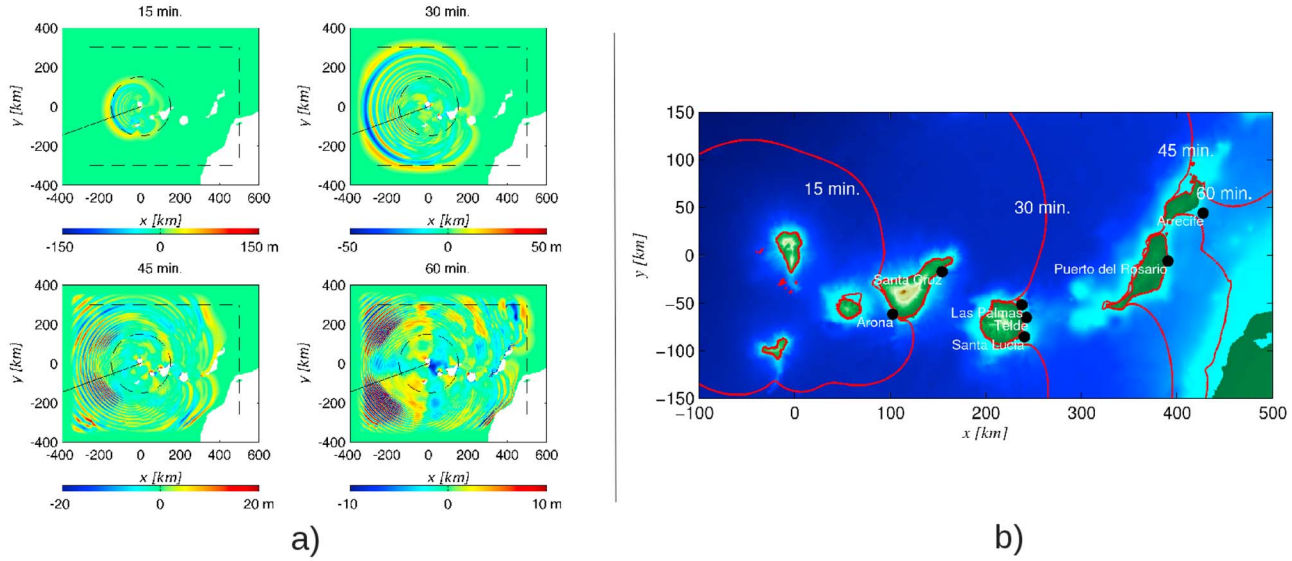

Figure 22. (a) Time sequence of FUNWAVE-TVD results. The dashed black lines indicate the boundary of the sponge layer in the model grid and the size of the initial THETIS grid. Solid black line indicates the location of transects. (b) Travel time for the 80 km^3 case to the different Canary Islands, noting the station locations used for inundation height measurements.

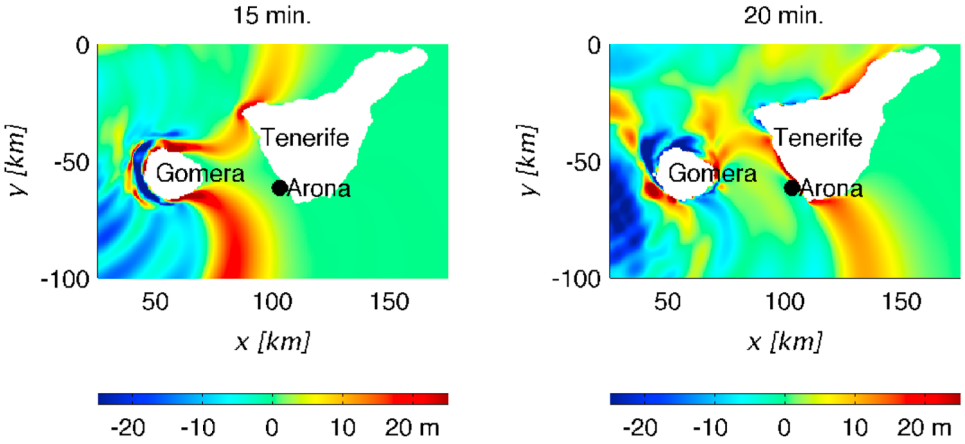

Figure 23. Near field impact of the 80 km^3 case, modeled with FUNWAVE-TVD in a 500 m resolution grid surrounding Tenerife, at (left) 15 min and (right) 20 min after the landslide.

2000 m results at Arona (Figure 24), on the southern coast of Tenerife, show that computed waves are very similar at all three resolutions. Using a long-wave inundation model with nested or adaptive grid refinement would be necessary to sufficiently resolve the inundation distances and runup heights; this could be the object of future work.

[38] For the 80 km^3 slide scenario (but this will also apply to all slide scenarios), tsunami propagation from La Palma across the Canary Islands takes about 1 h (Figure 22b). Waves first impact the Hierro coastline, which reflects significant energy in the process. At about the same time, waves wrap around Gomera and this refraction-diffraction causes increased wave height on the southwest side of Tenerife. The tsunami has lower wave heights on the north side, in comparison, because the island of La Palma somewhat protects against as much energy being sent directly east. After waves pass by Gran Canaria, they propagate almost unchanged toward the easternmost islands, impacting the length of Fuerteventura and Lanzarote almost simultaneously.

[39] Analyzing FUNWAVE-TVD results for the various stations, we compare in Table 1 the maximum wave height computed at each station, for the four different slide volume scenarios simulated. First, results in Table 1 favorably compare with earlier results of *Ward and Day* [2001] and *Løvholt et al.* [2008], although the specifics are slightly different in each case. While neither gives the precise locations of their measurements, Ward and Day (with a 500 km^3 slide) predicted a wave elevation around 61 m on the south side of Tenerife, and Løvholt et al. (with a 375 km^3 slide) predicted a 47 m wave elevation at their Tenerife West station; this can be compared to our 450 km^3 slide scenario, which yields a 54.8 m wave elevation at the Arona station on Tenerife. Oddly, the wave in Ward and Day's scenario takes 30 min to reach the southern edge of Tenerife, whereas in our results the wave has already reached Gran Canaria by this time (Figure 22a at 30 min.; Figure 22b). In Table 1, propagation times vary little with slide volume. Wave height, however, clearly increases with slide volume, but

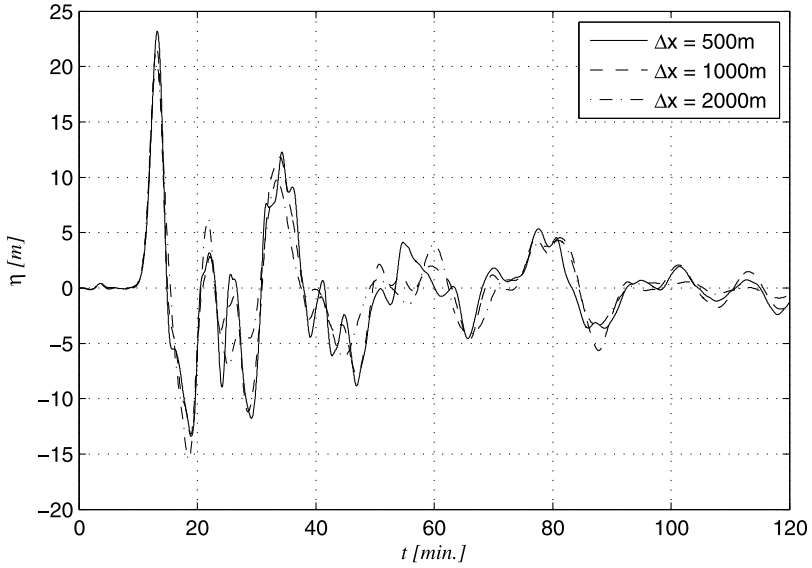

Figure 24. Time series of computed surface elevation at the Arona station, for different grid resolutions, from 500 to 2000 m.

Table 1. Maximum Wave Elevation at Seven Stations Around the Canary Islands[a]

Station	Location	Water Depth	Arrival Time	20 km^3	40 km^3	80 km^3	450 km^3
			Gran Canaria				
Las Palmas	28.128 N 15.385 W	139 m	37–38 min.	0.92 m	1.75 m	5.34 m	13.8 m
Telde	28.000 N 15.340 W	141 m	39–40 min.	2.96 m	5.73 m	7.93 m	20.1 m
Santa Lucia	27.820 N 15.370 W	64 m	36–38 min.	3.26 m	6.35 m	8.57 m	17.8 m
			Tenerife				
Santa Cruz	28.450 N 16.230 W	423 m	28–30 min.	3.27 m	6.72 m	9.36 m	20.5 m
Arona	28.060 N 16.760 W	204 m	17–18 min.	8.95 m	17.3 m	23.2 m	54.8 m
			Lanzarote				
Arrecife	28.930 N 13.420 W	1127 m	65–67 min.	0.70 m	1.38 m	1.97 m	4.98 m
			Fuerteventura				
Puerto del Rosario	28.490 N 13.820 W	182 m	59–60 min.	0.74 m	1.49 m	2.07 m	4.88 m

[a]The arrival time for the peak wave was essentially the same for the four test cases.

there does not seem to be a general relationship between these two parameters that applies for all of the stations.

4.4. Westward Wave Propagation

[40] Pending results of additional simulations of tsunami propagation across the Atlantic basin, FUNWAVE-TVD results can be used to quantify the initial decay with distance from La Palma of the maximum tsunami wave elevation. Similar to the THETIS results (Figure 14), this is done in vertical transects, such as Figure 25, which spans to 300 km or so in the same transect as before. Thus, using results in Figure 22a for the 4 earlier slide scenarios, we derived power laws representing the decay of the leading wave amplitude, computed every 5 min. for the first 25 min. of propagation. Using the same power law as before: $\eta = ar^b$, where r is the radial distance traveled by the wave, this yields the decay rates $b = -1.10$, -1.09, -1.08, and -1.02 (for the 20, 40, 80, and 450 km^3 scenarios, respectively). In each case, we

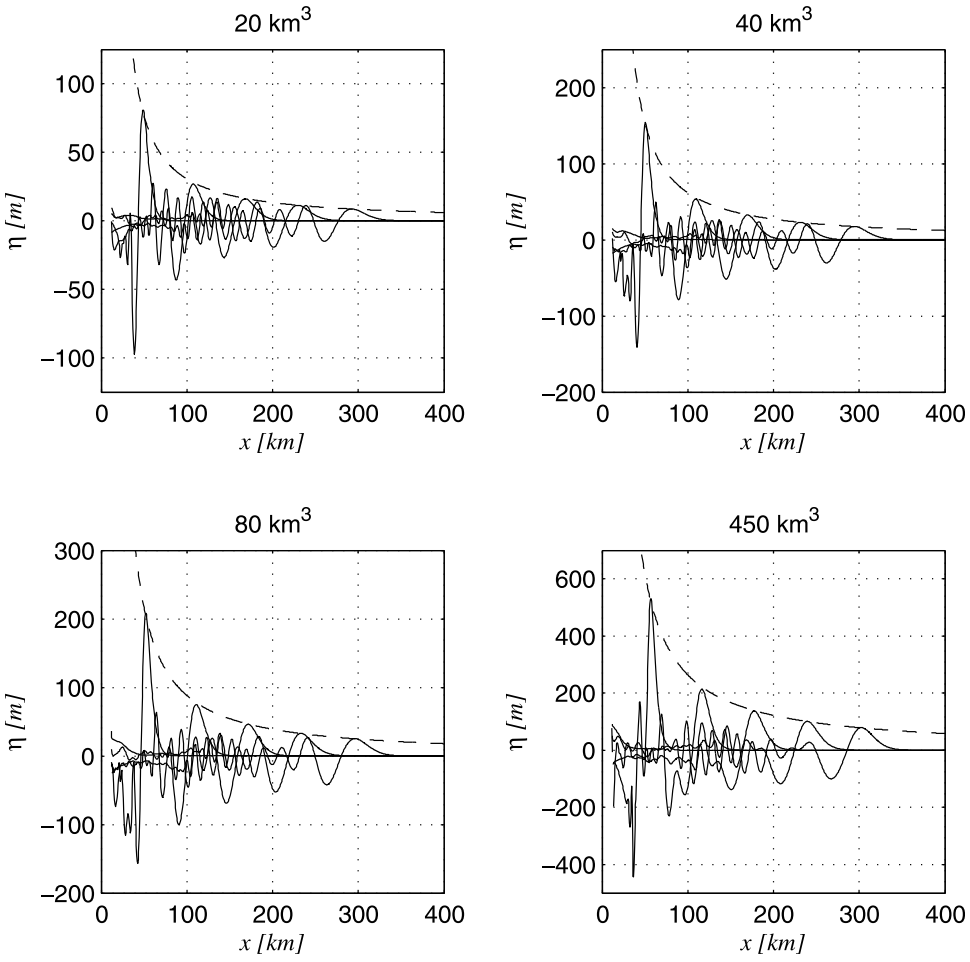

Figure 25. Transects (see Figure 19) of surface elevation as a function of the westward propagation distance of the tsunami caused by various slide volume scenarios. Power laws indicate the decay rate of maximum elevation: 20 km^3 case $- r^{-1.10}$; 40 km^3 case $- r^{-1.19}$; 80 km^3 $- r^{-1.08}$; 450 km^3 case $- r^{-1.02}$.

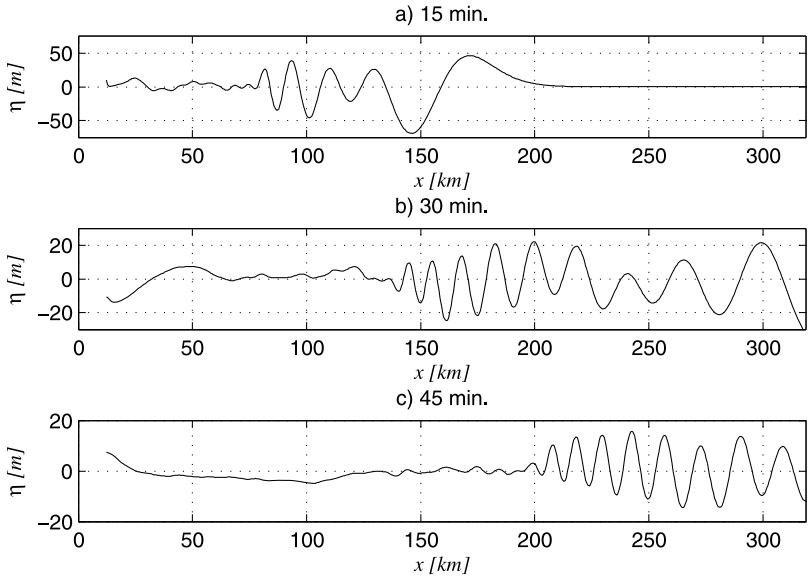

Figure 26. Transects (see Figure 19) of surface elevation, for the 80 km^3 slide, at t = (a) 15 min, (b) 30 min, and (c) 45 min as a function of propagation distance up to the edge of the sponge layer. Results show the long dispersive tail that gradually develops with time.

find that wave elevation decays slower than predicted in THETIS' results alone, for the early stages of propagation (first 100 km or so; Figure 14); this is expected as there is still a substantial amount of dissipation occurring throughout THETIS' simulations, not included in the BM. Finally, note that, except for the 450 km^3 case, the second wave becomes nearly as large as the leading wave after 25 min. of propagation, due to the initial stages of forming a dispersive tail. Even as this dispersive tail decreases in amplitude, it is still very large in comparison to the waves propagating toward the other Canary Islands (Figure 26).

[41] The westward tsunami propagation and far-field impact (in particular along the U.S. east coast) will be further studied and reported on, for the four selected CVV slide scenarios, beyond the stage of Figure 22a, as part of a follow up study to this work. However, current results already show notable differences with earlier results reported by *Ward and Day* [2001] and *Løvholt et al.* [2008]. In *Ward and Day* [2001] (with a 500 km^3 slide scenario), the maximum wave elevation after 30 min. from slide initiation was about 188 m, and it did not occur for the leading wave, which was substantially larger than that predicted in our 450 km^3 scenario. Løvholt et al. (personal communication, 2012) predicted a maximum wave elevation after 25 min. of about 48 m with a 375 km^3 slide scenario while we predict 79 m at the same time (i.e., just prior to reaching the sponge layer in FUNWAVE's grid) along the transect used above, for our larger 450 slide km^3 scenario. This may be due largely from the different slide models, instead of the wave modeling. At 300 s, *Løvholt et al.* [2008, Figure 3a] initiate their Boussinesq model with a wave approximately 250 m high, whereas for our present study our initial leading wave is 536 m high. Still, as discussed above, the specifics of numerical models used and their ability to accurately represent and resolve the physical processes at play, as well as the accuracy of the bathymetric and topographic data used near and around the Canary islands, may also play an important role in explaining these differences. As indicated, the important prediction of the far-field tsunami impact across the Atlantic (e.g., in North America), resulting from various CVV flank collapse scenario, and the analysis of associated tsunami coastal impact, will be detailed and reported on in future work.

5. Conclusions

[42] We presented a numerical study of tsunami wave generation by the Cumbre Vieja Volcano (CVV) flank collapse. A multifluid Navier-Stokes model, with a VOF interface tracking, was used to calculate the free surface elevation generated by deforming slide motion. Waves were then input as initial condition in a Boussinesq model, to study their propagation in the near field, around nearby islands. Such simulations include frequency dispersion effects, which are important for landslide generated waves, owing to their relatively shorter wavelength. Both of these numerical models have been fully validated in other work, for landslide tsunami generation and propagation.

[43] By contrast with other recent work that focused on the most extreme scenario, the current study considered several slide scenarios based on geotechnical slope stability analyses and a more accurate bathymetry. Additionally, the Navier-Stokes model used is different (incompressible).

[44] The main conclusions of our work are as follows:

[45] 1. The volume of the most unstable part of CVV should range between 40 and 80 km^3 (results from slope stability analyses are detailed in another paper), which is consistent with the order of magnitude of locally identified submarine debris avalanche deposits. Without any additional disturbing forces (such as seismic acceleration for instance), CVV's slope appears stable at the moment, as illustrated by a high factor of safety.

[46] 2. In each case (i.e., for four slide volumes of 20, 40, 80 and 450 km^3), generated wave trains share common

features: (1) A large positive elevation wave is first generated, which reaches a maximum of a few hundred meters. Such a high value is explained by the combination of a large slide volume and a slide Froude numbers close to one (i.e., critical regime); (2) This initial wave then rapidly decreases, spawning a few large trailing waves, which are propagating over a globally negative mean sea level; (3) The generated wave energy is maximum in a direction near 20–25° Southward of West; (4) The wavelength is around 22–27 km after about 7.5 min of propagation.

[47] 3. As could be expected, the maximum wave elevation is strongly dependent on the initial slide volume, varying between 600 to 1200 m with increasing slide volume, within the tested range.

[48] 4. The maximum wave impact was computed at several key locations in the Canary Islands. On La Palma, the town of Santa Cruz, on the lee side, would be struck by two simultaneous inundation waves with devastating consequences. Due to their location, El Hierro and Gomera, which fortunately are not densely populated, would also be strongly impacted. Despite the large or even extreme events considered, the expected consequences on the Canarian archipelago may be attenuated because the other Canary Islands are all situated Eastward of La Palma and the major towns and touristic areas are on the east sides of these Islands. Nevertheless important cities in Gran Canaria or Tenerife would be subjected to high tsunami impact for every considered scenario.

[49] 5. While our overall findings are qualitatively consistent with those of *Gisler et al.* [2006] and *Lovhølt et al.* [2008], waves computed in our study appear to be significantly higher than in these earlier works. In the near field the attenuation rates are smaller than those of Gisler *et al.*, whereas the far-field values are comparable to those of Løvholt et al. Hence, the consequences of our simulated events in terms of tsunami impact in the near- and also likely in the far-field would be somewhat larger. While the attenuation rates for moderate propagation distances (e.g., up to 300 km) are slightly larger than those found in the literature, we leave the detailed analysis of results on far-field effects of this tsunami for a future paper, as the complex physics involved (propagation and runup) requires a more comprehensive description.

[50] 6. On a methodological point of view, our 2D computations show that significant energy transfer from slide to wave motion only lasts for a short time (order 200 s). Therefore, both slide and fluid dynamics during this initial period must be very thoroughly and accurately simulated to ensure accurate tsunami forecasting, which justifies our choice of a highly resolved 3D-NS model to do so. Similarly, the location of the center of gravity of the unstable CVV slope volume has to be carefully selected as variations in this parameter were shown to have important effects on generated wave amplitudes.

[51] **Acknowledgments.** Partial funding for this work was provided by grant NA10NMS4670010 of NOAA's National Tsunami Hazards Mitigation Program (NTHMP), grant EAR-09-11499 of the U.S. National Science Foundation, and grant 037058 of the European Commission Tsunami Risk And Strategies For the European Region (TRANSFER) program. Stéphane Abadie was awarded an Aquitaine Fulbright grant, cofunded by the Aquitaine Region and the Fulbright commission, during his stay at University of Rhode Island. Numerical simulations were run on a 12-core Mac Pro cluster located at URI and funded by the NTHMP program, the 256-core "Elanion" cluster (ALTIX ICE 8200) co-funded by the Aquitaine Region and the 12,288- core "Jade" cluster of CINES. The authors also thank the Institut de Mécanique et d'Ingénierie de Bordeaux for the use of the "elanion" cluster and, more specifically, Stéphane Glockner for his support on technical and numerical aspects of the THETIS model. The authors finally wish to acknowledge the help of Tayebeh Tajallibakhsh for processing results of the 2D sensitivity analysis.

References

Abadie, S., J. P. Caltagirone, and P. Watremez (1998), Splash-up generation in a plunging breaker, *C. R. Acad. Sci., Ser. IIB*, *326*(9), 553–559.

Abadie, S., C. Gandon, S. Grilli, R. Fabre, J. Riss, E. Tric, D. Morichon, and S. Glockner (2008), 3D numerical simulations of waves generated by subaerial mass failures: Application to La Palma case, in *Proceedings of the 31st International Coastal Engineering Conference*, edited by J. Mc Kee Smith, pp. 1384–1395, World Sci., Singapore.

Abadie, S., D. Morichon, S. Grilli, and S. Glockner (2010), Numerical simulation of waves generated by landslides using a multiple-fluid Navier-Stokes model, *Coastal Eng.*, *57*, 779–794, doi:10.1016/j.coastaleng.2010.03.003.

Abadie, S., J. Harris, and S. Grilli (2011), Numerical simulation of tsunami generation by the potential flank collapse of the Cumbre Vieja volcano, paper presented at 21st Offshore and Polar Engineering Conference, Int. Soc. of Offshore and Polar Eng., Maui, Hawaii, 19–24 June.

Carracedo, J., S. Day, H. Guillou, and P. Gravestock (1999), Later stage of volcanic evolution of La Palma, Canary Islands: Rift evolution, giant landslides, and the genesis of the Caldera de Taburiente, *Geol. Soc. Am. Bull.*, *111*, 755–768, doi:10.1130/0016-7606(1999)111<0755:LSOVEO>2.3.CO;2.

Cecioni, C., and G. Bellotti (2010), Inclusion of landslide tsunamis generation into a depth integrated wave model, *Nat. Hazards Earth Syst. Sci.*, *10*, 2259–2268, doi:10.5194/nhess-10-2259-2010.

Chen, Q. (2006), Fully nonlinear Boussinesq-type equations for waves and currents over porous beds, *J. Eng. Mech.*, *132*, 220–230, doi:10.1061/(ASCE)0733-9399(2006)132:2(220).

Chen, Q., J. T. Kirby, R. A. Dalrymple, A. B. Kennedy, and A. Chawla (2000), Boussinesq modeling of wave transformation, breaking, and runup. II: 2-D. *J. Waterw. Port Coastal Ocean Eng.*, *126*(1), 48–56.

Chen, Q., J. T. Kirby, R. A. Dalrymple, F. Shi, and E. B. Thornton (2003), Boussinesq modeling of longshore currents, *J. Geophys. Res.*, *108*(C11), 3362, doi:10.1029/2002JC001308.

Cochonat, P., et al. (1990), Importance des dépôts gravitaires dans la mise en place d'un système volcano-sédimentaire sous-marin (Volcan de la Fournaise, Ile de la Réunion). *C. R. Acad. Sci., Ser. IIB*, *311*, 679–686.

Day, S. J., P. Watts, S. T. Grilli, and J. T. Kirby (2005), Mechanical models of the 1975 Kalapana, Hawaii, earthquake and tsunami, *Mar. Geol.*, *215*(1–2), 59–92, doi:10.1016/j.margeo.2004.11.008.

Enet, F., and S. Grilli (2007), Experimental study of tsunami generation by three-dimensional rigid underwater landslides. *J. Waterw. Port Coastal Ocean Eng.*, *133*(6), 442–454.

Fine, I. V., A. B. Rabinovitch, R. E. Thomson, and E. A. Kulikov (2003), Numerical simulation of tsunami generation by submarine and subaerial landslides, in *Submarine Landslides and Tsunamis*, pp. 69–88, Kluwer Acad., Dordrecht, Netherlands, doi:10.1007/978-94-010-0205-9_9.

Fritz, H. M., W. H. Hager, and H. E. Minor (2004), Near field characteristics of landslide generated impulse waves, *J. Waterw. Port Coastal Ocean Eng.*, *130*(6), 287–302, doi:10.1061/(ASCE)0733-950X(2004)130:6(287).

Fuhrman, D. R., and P. A. Madsen (2009), Tsunami generation, propagation, and run-up with a high-order Boussinesq model, *Coastal Eng.*, *56*, 747–758, doi:10.1016/j.coastaleng.2009.02.004.

Giachetti, T., R. Paris, K. Kelfoun, and F. J. Pérez-Torrado (2011), Numerical modelling of the tsunami triggered by the Güimar debris avalanche, Tenerife (Canary Islands): Comparison with field-based data, *Mar. Geol.*, *284*(1–4), 189–202, doi:10.1016/j.margeo.2011.03.018.

Gisler, G. R. (2008), Tsunami simulations, *Annu. Rev. Fluid Mech.*, *40*, 71–90, doi:10.1146/annurev.fluid.40.111406.102208.

Gisler, G., R. Weaver, and M. Gittings (2006), SAGE calculations of the tsunami threat from La Palma, *Sci. Tsunami Hazards*, *24*, 288–301.

Goda, K. (1979), A multi-step technique with implicit difference schemes for calculating two- or three-dimensional cavity flows, *J. Comput. Phys.*, *30*, 76–95, doi:10.1016/0021-9991(79)90088-3.

Grilli, S. T., and P. Watts (1999), Modeling of waves generated by a moving submerged body: Applications to underwater landslides, *Eng. Anal. Boundary Elem.*, *23*, 645–656, doi:10.1016/S0955-7997(99)00021-1.

Grilli, S. T., and P. Watts (2005), Tsunami generation by submarine mass failure: 1. Modeling, experimental validation, and sensitivity analysis, *J. Waterw. Port Coastal Ocean Eng.*, *131*(6), 283–297, doi:10.1061/(ASCE)0733-950X(2005)131:6(283).

Grilli, S. T., S. Vogelmann, and P. Watts (2002), Development of a 3D numerical wave tank for modeling tsunami generation by underwater landslides, *Eng. Anal. Boundary Elem.*, *26*(4), 301–313, doi:10.1016/S0955-7997(01)00113-8.

Grilli, S. T., C. D. P. Baxter, S. Maretzki, Y. Perignon, and D. Gemme (2006), Numerical simulation of tsunami hazard maps for the US East Coast, report, 34 pp., FMGlobal Proj., Univ. of Rhode Island, Narragansett.

Grilli, S. T., M. Ioualalen, J. Asavanant, F. Shi, J. Kirby, and P. Watts (2007), Source constraints and model simulation of the December 26, 2004 Indian Ocean Tsunami, *J. Waterw. Port Coastal Ocean Eng.*, *133*(6), 414–428, doi:10.1061/(ASCE)0733-950X(2007)133:6(414).

Grilli, S. T., S. Dubosq, N. Pophet, Y. Perignon, J. T. Kirby, and F. Shi (2010), Numerical simulation and first-order hazard analysis of large co-seismic tsunamis generated in the Puerto Rico trench: Near-field impact on the North shore of Puerto Rico and far-field impact on the US East Coast, *Nat. Hazards Earth Syst. Sci.*, *10*, 2109–2125, doi:10.5194/nhess-10-2109-2010.

Grilli, S. T., J. C. Harris, T. Tajalibakhsh, T. L. Masterlark, C. Kyriakopoulos, J. T. Kirby, and F. Shi (2012), Numerical simulation of the 2011 Tohoku tsunami based on a new transient FEM co-seismic source: Comparison to far- and near-field observations, *Pure Appl. Geophys.*, in press.

Harbitz, C. B. (1992), Model simulations of tsunamis generated by the Storegga slides, *Mar. Geol.*, *105*, 1–21, doi:10.1016/0025-3227(92)90178-K.

Hirt, C. W., and B. D. Nichols (1981), Volume of fluid (VOF) method for the dynamics of free boundaries, *J. Comput. Phys.*, *39*(1), 201–225, doi:10.1016/0021-9991(81)90145-5.

Holcomb, R. T., and R. C. Searle (1991), Large landslides from oceanic volcanoes, *Mar. Geotechnol.*, *10*, 19–32, doi:10.1080/10641199109379880.

Hungr, O. (1995), A model for the runout analysis of rapid flow slides, debris flows, and avalanches, *Can. Geotech. J.*, *32*, 610–623, doi:10.1139/t95-063.

Inoue, K. (1999), Shimabara-Shigatusaku earthquake and topographic changes by Shimabara Catastrophe in 1792, *J. Jpn. Soc. Erosion Control Eng.*, *52*, 45–54.

Ioualalen, M., J. Asavanant, N. Kaewbanjak, S. T. Grilli, J. T. Kirby, and P. Watts (2007), Modeling the 26th December 2004 Indian Ocean tsunami: Case study of impact in Thailand, *J. Geophys. Res.*, *112*, C07024, doi:10.1029/2006JC003850.

Jiang, L., and P. H. Leblond (1992), The coupling of a submarine slide and the surface wave it generates, *J. Geophys. Res.*, *97*(12), 731–744.

Jiang, L., and P. H. Leblond (1993), Numerical modeling of an underwater Bingham plastic mudslide and the wave which it generates, *J. Geophys. Res.*, *98*, 10,303–10,317, doi:10.1029/93JC00393.

Kelfoun, K., and T. H. Druitt (2005), Numerical modelling of the emplacement of Socompa rock avalanche, Chile, *J. Geophys. Res.*, *110*, B12202, doi:10.1029/2005JB003758.

Kelfoun, K., T. Giachetti, and P. Labazuy (2010), Landslide-generated tsunamis at Reunion Island, *J. Geophys. Res.*, *115*, F04012, doi:10.1029/2009JF001381.

Kelfoun, K., T. Giachetti, P. Labazuy, and R. Paris (2011), Landslide-generated tsunamis at Reunion Island and their possible sedimentary record in Mauritius Island, paper presented at General Assembly 2011, Eur. Geosci. Union, Vienna.

Kennedy, A. B., Q. Chen, J. T. Kirby, and R. A. Dalrymple (2000), Boussinesq modeling of wave transformation, breaking, and runup. I: 1D, *J. Waterw. Port Coastal Ocean Eng.*, *126*(1), 39–47.

Kirby, J. T. (2003), Boussinesq models and applications to nearshore wave propagation, surf zone processes and wave-induced currents, in *Advances in Coastal Modeling*, *Oceanogr. Ser.*, vol. 67, edited by V. C. Lakhan, pp. 1–41, Elsevier, New York, doi:10.1016/S0422-9894(03)80118-6.

Legros, F. (2002), The mobility of long-runout landslides, *Eng. Geol.*, *63*(3–4), 301–331, doi:10.1016/S0013-7952(01)00090-4.

LeVeque, R. J. (1992), *Numerical Methods for Conservation Laws*, Birkhauser, Zurich, doi:10.1007/978-3-0348-8629-1.

Liu, P. L. F., T. R. Wu, F. Raichlen, C. E. Synolakis, and J. C. Borrero (2005), Runup and rundown generated by three-dimensional masses, *J. Fluid Mech.*, *536*, 107–144, doi:10.1017/S0022112005004799.

Løvholt, F., G. Pedersen, and G. Gisler (2008), Oceanic propagation of a potential tsunami from the La Palma Island, *J. Geophys. Res.*, *113*, C09026, doi:10.1029/2007JC004603.

Lubin, P., S. Vincent, S. Abadie, and J. P. Caltagirone (2006), Three-dimensional large eddy simulation of air entrainment under plunging breaking waves, *Coastal Eng.*, *53*(8), 631–655, doi:10.1016/j.coastaleng.2006.01.001.

Lynett, P., and P. L.-F. Liu, (2003), A numerical study of submarine-landslide-generated waves and runup, *Proc. R. Soc. A*, *458*, 2885–2910.

Mader, C. L. (2001), Modeling the La Palma landslide tsunami, *Sci. Tsunami Hazards*, *19*, 150–170.

Mård Karlsson, J. M., A. Skelton, M. Sanden, M. Ioualalen, N. Kaewbanjak, N. Pophet, J. Asavanant, and A. von Matern (2009), Reconstructions of the coastal impact of the 2004 Indian Ocean tsunami in the Khao Lak area, Thailand, *J. Geophys. Res.*, *114*, C10023, doi:10.1029/2009JC005516.

Masson, D., A. Watts, M. Gee, R. Urgeles, N. Mitchell, T. Le Bas, and M. Canals (2002), Slope failures on the flanks of the western Canary Islands, *Earth Sci. Rev.*, *57*, 1–35, doi:10.1016/S0012-8252(01)00069-1.

McMurtry, G. M., P. Watts, G. J. Fryer, J. R. Smith, and F. Imamura (2004), Giant landslides, mega-tsunamis, and paleo-sea level in the Hawaiian Islands, *Mar. Geol.*, *203*, 219–233, doi:10.1016/S0025-3227(03)00306-2.

McMurtry, G. M., D. R. Tappin, P. N. Sedwick, I. Wilkinson, J. Fietzke, and B. Sellwood (2007), Elevated marine deposits in Bermuda record a late Quaternary megatsunami, *Sediment. Geol.*, *200*(3–4), 155–165, doi:10.1016/j.sedgeo.2006.10.009.

Montagna, F., G. Bellotti, and M. Di Risio (2011), 3D numerical modeling of landslide-generated tsunamis around a conical island, . *Nat Hazards*, *58*, 591–608, doi:10.1007/s11069-010-9689-0.

Moore, J. G., D. A. Clague, R. T. Holcomb, P. W. Lipman, W. R. Normark, and M. E. Torresan (1989), Prodigious submarine landslides on the Hawaiian Ridge, *J. Geophys. Res.*, *94*, 17465–17484, doi:10.1029/JB094iB12p17465.

Morichon, D., and S. Abadie (2010), Vague générée par un glissement de terrain, influence de la forme initiale et de la loi de déformabilité du glissement, *Houille Blanche*, *1*, 111–117, doi:10.1051/lhb/2010013.

Oehler, J. F., P. Labazuy, and J. F. Lénat (2004), Recurrence of major flank landslides during the last 2 Ma—History of Réunion Island, *Bull. Volcanol.*, *66*, 585–598, doi:10.1007/s00445-004-0341-2.

Pararas-Carayannis, G. (2002), Evaluation of the threat of mega tsunamis generation from postulated massive slope failures of island stratovolcanoes on La Palma, Canary Islands, and on the island of Hawaii, *Sci. Tsunami Hazards*, *20*, 251–277.

Paris, R., J. C. Carracedo, and F. J. Pérez-Torrado (2005), Massive flank failures and tsunamis in the Canary Islands: Past, present, future, *Z. Geomorphol.*, *140*, Suppl., 37–54.

Pérez-Torrado, J. F., R. Paris, M. Cabrera, J. L. Schneider, P. Wassmer, J. C. Carracedo, A. Rodriguez-Santana, and F. Santana (2006), Tsunami deposits related to flank collapse in oceanic volcanoes: The Agaete Valley evidence, Gran Canaria, Canary Islands, *Mar. Geol.*, *227*, 135–149, doi:10.1016/j.margeo.2005.11.008.

Pérignon, Y. (2006). Tsunami hazard modeling, MSc thesis, Univ. of Rhode Island, Narragansett.

Quecedo, M., M. Pastor, and M. I. Herreros (2004), Numerical modelling of impulse wave generated by fast landslides, *Int. J. Numer. Methods Eng.*, *59*, 1633–1656, doi:10.1002/nme.934.

Robinson, J. E., and B. W. Eakins (2006), Calculated volumes of individual shield volcanoes at the young end of the Hawaiian Ridge, in *Growth and Collapse of Hawaiian Volcanoes*, edited by M. L. Coombs, B. W. Eakins, and P. F. Cervelli, *J. Volcanol. Geotherm. Res.*, *151*, 309–317.

Ryan, W. B. F., et al. (2009), Global multi-resolution topography synthesis, *Geochem. Geophys. Geosyst.*, *10*, Q03014, doi:10.1029/2008GC002332.

Shi, F., J. T. Kirby, J. C. Harris, J. D. Geiman, and S. T. Grilli (2012), A high-order adaptive time-stepping TVD solver for Boussinesq modeling of breaking waves and coastal inundation, *Ocean Modell.*, *43–44*, 36–51, doi:10.1016/j.ocemod.2011.12.004.

Tappin, D. R., P. Watts, and S. T. Grilli (2008), The Papua New Guinea tsunami of 1998: Anatomy of a catastrophic event, *Nat. Hazards Earth Syst. Sci.*, *8*, 243–266, doi:10.5194/nhess-8-243-2008.

Tinti, S., A. Manucci, G. Pagnoni, A. Armigliato, and F. Zaniboni (2005), The 30th December 2002 landslide-induced tsunami in Stromboli: Sequence of the events reconstructed from eyewitness accounts, *Nat. Hazards Earth Syst. Sci.*, *5*, 763–775, doi:10.5194/nhess-5-763-2005.

van der Vorst, H. A. (1992), BI-CGSTAB: A fast and smoothly converging variant of BI-CG for the solution of nonsymmetric linear systems, *SIAM J. Sci. Stat. Comput.*, *13*, 631–644, doi:10.1137/0913035.

Vincent, S., and J.-P. Caltagirone (1999), Efficient solving method for unsteady in-compressible interfacial flow problems, *Int. J. Numer. Methods Fluids*, *30*, 795–811, doi:10.1002/(SICI)1097-0363(19990730)30:6<795::AID-FLD872>3.0.CO;2-2.

Ward, S. N., and S. Day (2001), Cumbre Vieja Volcano—Potential collapse and tsunami at La Palma, Canary Islands, *Geophys. Res. Lett.*, *28*, 3397–3400, doi:10.1029/2001GL013110.

Watts, A. B. (2000), Tsunami feature of solid block underwater landslides, *J. Waterw. Port Coastal Ocean Eng.*, *126*(3), 127–137.

Watts, A. B., and D. G. Masson (1995), A giant landslide on the north flank of Tenerife, Canary Islands, *J. Geophys. Res.*, *100*(B12), 24,487–24,498.

Watts, P., S. T. Grilli, J. T. Kirby, G. J. Fryer, and D. R. Tappin (2003), Landslide tsunami case studies using a Boussinesq model and a fully nonlinear tsunami generation model, *Nat. Hazards Earth Syst. Sci.*, *3*, 391–402, doi:10.5194/nhess-3-391-2003.

Watts, P., S. T. Grilli, D. Tappin, and G. J. Fryer (2005), Tsunami generation by submarine mass failure Part II: Predictive equations and case studies, *J. Waterw. Port Coastal Ocean Eng.*, *131*(6), 298–310, doi:10.1061/(ASCE)0733-950X(2005)131:6(298).

Wei, G., J. T. Kirby, S. T. Grilli, and R. Subramanya (1995), A fully nonlinear Boussinesq model for free surface waves. Part I: Highly nonlinear unsteady waves, *J. Fluid Mech.*, *294*, 71–92, doi:10.1017/S0022112095002813.

Weiss, R., H. M. Fritz, and K. Wuennemann (2009), Hybrid modeling of the mega-tsunami runup in Lituya Bay after half a century, *Geophys. Res. Lett.*, *36*, L09602, doi:10.1029/2009GL037814.

Wynn, R. B., and D. G. Masson (2003), Canary island landslides and tsunami generation: Can we use turbidite depositis to interpret landslide processes, in *Submarine Mass Movements and Their Consequences*, edited by J. Locat and J. Mienert, pp. 325–332, Kluwer Acad., Dordrecht, Netherlands.

Youngs, D. L. (1982), Time-dependent multimaterial flow with large fluid distortion, in *Numerical Methods for Fluid Dynamics*, edited by K. Morton and M. Baines, pp. 273–285, Academic, San Diego, Calif.

Zhou, H., and M. H. Teng (2010), Extended fourth-order depth-integrated model for water waves and currents generated by submarine landslides, *J. Eng. Mech.*, *136*(4), 506–516, doi:10.1061/(ASCE)EM.1943-7889.0000087.

Zhou, H., C. W. Moore, Y. Wei, and V. V. Titov (2011), A nested-grid Boussinesq type approach to modelling dispersive propagation and runup of landslide generated tsunamis, *Nat. Hazards Earth Syst. Sci.*, *11*(10), 2677–2697, doi:10.5194/nhess-11-2677-2011.